Sustainable Energy & Fuels

ROYAL SOCIETY OF CHEMISTRY

PAPER

View Article Online
View Journal

Cite this: DOI: 10.1039/d3se00649b

Ni/Co in and on CeO_2: a comparative study on the dry reforming reaction†

Pradeep Kumar Yadav, Kalyani Patrikar, Anirban Mondal and Sudhanshu Sharma *

Received 17th May 2023
Accepted 3rd July 2023

DOI: 10.1039/d3se00649b

rsc.li/sustainable-energy

Mono metal (Ni, Co)-substituted (in) and supported (on) CeO_2 catalysts were prepared by using solution combustion synthesis and formaldehyde reduction methods. The catalysts were completely characterized by both bulk and surface techniques. Both supported and substituted catalysts show distinct differences in the dry reforming of methane (DRM) activity. Co-substituted CeO_2 showed the highest stability under the DRM reaction conditions at 800 °C. Detailed kinetic investigations were also carried out to estimate the apparent activation energy. Carbon deposition on the spent catalysts was investigated by thermal gravimetric analysis (TGA) and TEM which shows that the deactivation is due to the presence of amorphous and graphitic carbon. Transient studies on a mass spectrometer indicate that the prominence of the reaction $CO_2 + C \rightarrow 2CO$ is responsible for the catalyst's stability. Surface lattice oxygen reactivity is a vital factor in catalytic stability and its action decides the reaction steps. DFT further verifies that the energy of vacancy formation is significantly lower in Co-substituted CeO_2 as compared to Ni-substituted CeO_2. This confirms that the Co-substituted catalyst favors oxidation due to higher availability of surface oxygen, while in contrast Ni hinders oxidation by decreasing the availability of surface oxygen for the reaction.

1 Introduction

Global warming has sent alarming threats to humanity[1] through various natural calamities and has become a significant concern in this modern era. The major contributors to global warming are greenhouse gases[2–5] like methane (CH_4) and carbon dioxide (CO_2)[6]. To counter these problems, various methods are being investigated. One of the most promising of them is dry reforming, which is a process to convert CO_2 and CH_4 (1 : 1) into valuable products like syn-gas[7,8] (H_2 + CO) (1 : 1). Syngas can be used for power generation and can produce many valuable chemicals using the Fischer–Tropsch process.[7,9–15] The process of DRM occurs spontaneously only at extremely high temperatures in the range of 800–1200 °C, which makes it economically non-viable; that's why catalysis of DRM has been an area of utmost importance. However, certain aspects still need to be solved. The main limitations of the DRM reaction are: (i) the deactivation of the catalyst at high temperature due to carbon deposition/coke[16–25] formation on the surface of the catalyst (ii) sintering of the catalyst, *i.e.*, blockage of active sites on the catalyst's surface[15,24,26–28] mainly due to the decomposition of methane, and the Boudouard reaction and other side reactions like the reverse water-gas shift reaction[29] which compete with DRM in its operational temperature range and thereby decreasing the expected output ratio of syngas.

Noble metals such as Pt, Rh, Ru, Ir, and others have shown excellent catalytic activity for DRM.[11,21,30–34] Over the years, efforts have been made to replace the expensive and rare noble metal-based catalysts with naturally abundant non-noble metals like Ni, Co, Cu, Zn, *etc.*, based catalysts,[35–37] which have shown promising results towards catalyzing the DRM reaction. Ni especially has exhibited great potential for catalyzing the process, but its activity significantly reduces due to coke deposition at high temperature.[38–40]

The current DRM research focuses on developing catalysts that have high resistance to coke deposition and sintering at high temperatures. The most popular catalyst system involves a non-noble metal as the active species, a support/host oxide to facilitate oxygen supply for the reaction, and a catalyst promoter.[41–44] Ceria (CeO_2) is being widely investigated as a support due to its redox properties, *i.e.*, its flexibility to switch between Ce^{3+} and Ce^{4+} oxidation states.[31,41] CeO_2's special feature is the release of lattice oxygen from the surface or bulk, which results in oxygen vacancies on the catalyst's surface.[41] During the dry reforming reaction, the oxygen formed due to CO_2 decomposition might fill up/adsorb on the oxygen vacancies in the lattice sites of CeO_2, which helps reduce the carbonaceous deposition on the surface of the catalyst.[45–53] In recent years, many oxide-based catalysts like MgO–ZrO_2, Al_2O_3,

Department of Chemistry, Indian Institute of Technology Gandhinagar, Gandhinagar 382355, India. E-mail: ssharma@iitgn.ac.in

† Electronic supplementary information (ESI) available. See DOI: https://doi.org/10.1039/d3se00649b

$MgAl_2O_4$, CeO_2, CeO_2–ZrO_2, *etc.*, have been developed.[31,43,54,55] The modern methods also include developing bimetallic/trimetallic catalysts where more than one metal works as an active species.[56–58] Such catalysts have shown better results for catalyzing the DRM reaction.

Although various models or hypotheses have been offered to explain the performance of La, Zr, Pr, Ti, *etc.* substituted CeO_2 (ref. 47–53) with Ni- and Co-based catalysts[59,60] for the DRM reaction Ni and Co as monometal substitution in the CeO_2 has not been examined in great depth.[61] The structural and chemical state evolution of these catalysts during DRM has not been thoroughly studied. Besides, whether a metal in the bulk substituted state is more active than when just present on the surface is also a big question. This is an important question because it is always tough to quantify if all the metal is present in the substituted state or part of it is on the surface. So, for that we have done a study comparing the DRM activity of two categories of catalysts: metal-substituted and metal-supported/deposited CeO_2. The focus is on reducing the catalyst deactivation to improve long-term stability, increasing the yield of the reaction, and improving the H_2/CO ratio. First, we have prepared 15 atom percent (randomly chosen concentration) of Ni and Co substituted into CeO_2 using the solution-combustion method,[62] as well as Ni and Co supported over CeO_2 catalysts using the chemical reduction method.[63,64] The hypothesis behind our approach is that Ni/Co substitution in CeO_2 causes the lattice oxygen activation and possibly the vacancy formation due to size and charge imbalance and this effect should affect the DRM activity in comparison to the Ni/Co supported CeO_2 where such an effect is missing. Experimental data show that substitution indeed affects the DRM activity in comparison to the supported catalyst on the parameters of conversion, product yield and stability under the gas stream and it has a strong link with the surface lattice oxygen. All of these modifications stand out more clearly in the case of Co-substituted CeO_2 than Ni-substituted CeO_2. These experimental observations are supported by first principal computations where it is shown that substitution by Co facilitates oxidation by increasing the availability of surface oxygen for the reaction, while it is hindered in the presence of Ni.

2 Experimental

2.1 Catalyst preparation

2.1.1. Metal-substituted CeO_2 catalysts using the solution-combustion method. This method involves a metal precursor and a fuel (reducer) which is generally an organic compound that can react with the metal precursor (oxidant) to start the combustion process at low ignition temperatures (300–450 °C). Here, we have used nitrate salts as precursors for metal because nitrates quickly leave as volatile gases like N_2 and NO_x. Following are the different precursors used: $[Ni(NO_3)_2\cdot 6H_2O]$ for nickel, $[Co(NO_3)_2\cdot 6H_2O]$ for cobalt, $[(NH_4)_2Ce(NO_3)_6]$ for cerium and oxalyldihydrazide [$NH_2NHCOCONHNH_2$, ODH] as the fuel or oxidizer. ODH is used as fuel due to its high reducing power and excellent chelating ability with the metal ion in solution. For the preparation of 15% atomic wt% Ni substituted in CeO_2, 5 g of ceric ammonium nitrate (CAN), 0.46 g of $[Ni(NO_3)_2\cdot 6H_2O]$ and 2.77 g of ODH are taken. For the preparation of 15% atomic wt% Co substituted in CeO_2 (Co–CeO_2), 5 g of ceric ammonium nitrate (CAN), 0.46 g $[Co(NO_3)_2\cdot 6H_2O]$ and 2.77 g of ODH are taken. Metal precursors and ODH (amounts of both are calculated using the valence factor method) are mixed in the least amount of ultra-pure water (approx. 20 mL) in a borosilicate crystallizing bowl. 2 mL of 1 M HNO_3 are added to obtain a clear homogeneous solution if needed and the mixture is placed in a muffle furnace at 450 °C; combustion occurs due to the highly exothermic redox reactions between the metal precursors and ODH finally giving a colored powder.

2.1.2 Metal deposition on a support (CeO_2) using the reduction method. Here, the weight percent of all the active metal components was equal to the substituted compounds. In addition, the CeO_2 support was synthesized using solution combustion. For the preparation of Ni supported over CeO_2 (Ni/CeO_2), 1 g CeO_2 and 0.34 g of $[Ni(NO_3)_2\cdot 6H_2O]$ were taken. The same was taken for Co supported over CeO_2 (Co/CeO_2); 1.0 g CeO_2 and 0.34 g of $[Co(NO_3)_2\cdot 6H_2O]$. Here, 1.0 g of the pre-prepared CeO_2 support was mixed in 40 mL of ethylene glycol ($C_2H_6O_2$) and the mixture was ultrasonicated for 30 min to obtain a homogeneous solution, followed by adding 1 M HNO_3 until pH becomes one. After adding 10 mL of acetone drop by drop, the solution was agitated for one hour. In the next step, Ni, Co salt solutions prepared in ultra-pure water were mixed with the support solution in separate beakers. 20 mL of formaldehyde (reducing agent) was then added dropwise with continuous stirring and afterwards the pH was adjusted to 10 using 5 wt% KOH. The resultant solution was mixed at room temperature for 30 minutes, followed by continuous stirring for 8 hours at 80 °C. In the last step, the solution was centrifuged at 10 000 rpm to obtain a residue, washed 3–4 times with ultra-pure water, and dried for 24 h. A final drying step at 120 °C yielded our desired catalyst in solid powder form.

2.2 Catalyst characterization

2.2.1 X-ray diffraction study. X-ray diffraction using a BRUKER D8 DISCOVER model demonstrated the crystallization of monometallic substituted and supported oxides. Cu K radiation (λ = 1.5406 Å) was utilized by the diffractometer to create diffraction patterns. Signals were collected for 2θ between 20 and 75° (step size = 0.40 steps per second and increment = 0.001). The crystallite size was calculated using the Debye–Scherrer equation. On the basis of the Rietveld technique, the JANA 2006 program was used to refine XRD patterns.

2.2.2 Surface area measurement and analysis. Using a Micromeritics Flex-3500 surface analyzer, the specific surface area, total pore volume, and pore size distribution of all fresh catalysts were measured at −196 °C. All samples were activated according to the following pre-treatment methodology prior to measurement. Initially, the samples were left at 100 °C for one hour in a N_2 atmosphere, followed by a three-hour stay at 150 °C (heating ramp 5 °C min^{-1}) using a Micromeritics Smart Prep degasser. The specific surface area of the samples was calculated using the Brunauer–Emmett–Teller (BET) technique. The pore size distribution was calculated using the Barrett–Joyner–

Halenda (BJH) approach from the desorption branch of the isotherms. At a relative pressure ratio of 0.99, the total pore volume was computed.

2.2.3 X-ray photoelectron spectroscopy (XPS). X-ray photoelectron spectroscopy (XPS) studies were conducted on the fresh catalysts using an Axis Ultra DLD spectrometer (Kartos) with monochromatic Al K radiation (1486.6 eV, line width 0.8 eV). The pressure in the analyzing chamber was maintained at 10^{-9} torr while the spectra were recorded. The apparatus provided information regarding the sample's surface layers or thin-film structures (the top 10–100 Å). Regarding C (1s), all binding energies were adjusted to 285.0 eV. Using the CASA software, the spectrum was deconvoluted with an accuracy of 0.2 eV. A U2 Tougaard was employed as the background for the deconvolution.

2.2.4 Thermal gravimetric analysis (TGA). The thermogravimetric analysis (TGA) of spent catalysts was carried out on NETZSCH STA 449 F3 Jupiter-DTA apparatus (alumina crucibles) with the purge gas (N_2) flow rate of 30 mL min^{-1} for sometime to remove the moisture and adsorbed species at 150 °C. The amount of carbon deposited on the samples was determined using an oxygen–nitrogen mixture (21 : 79) with a flow rate of 30 mL min^{-1}. The heating rate was 10 °C min^{-1} and the range was from 50 to 1000 °C.

2.2.5 Transmission electron microscopy (TEM). TEM analysis was performed over the freshly prepared catalysts as well as the spent catalysts after the 5 h catalytic run. The morphology of deposited carbon on the spent catalyst after the reaction was determined using an FEI Themis 60–300 with an EDS detector and FEI CETA 4k × 4k camera. Before performing the TEM analysis, the catalysts were dispersed ultrasonically in methanol. A drop of dispersion was drop-cast over the carbon-coated copper grid and dried for two days. J image software was used to measure the particle size and *d*-spacing, and for the SAED analysis of catalysts.

2.2.6 Catalytic evaluation. A fixed bed microreactor was used to further investigate the catalytic potential of dry reforming methane with carbon dioxide to generate H_2/CO (syngas). The reactor was coupled to an online gas chromatograph (GC) (Dhruva CIC Vadodara) with PORAPAK-N and PORAPAK-Q columns and a mass flow controller (Alicat). The gas chromatograph (GC) had both a TCD and FID detector. 100 mg of catalyst of granule size (180–300 micrometer) were used (to minimize the mass transport effect) and bed length was found 2 cm. The catalyst granules were packed within the quartz tube (OD 4 mm, length 25 cm) using quartz wool. In order to determine the temperature of the catalyst bed, a K-type thermocouple was used. The feed, a gas combination of $CH_4/CO_2/N_2$ = 1/1/18, was pumped at a rate of 20 mL min^{-1} from 25 °C to 800 °C (1 atm, GHSV = 12 000 mL g^{-1} h^{-1}) in order to undergo a dry reforming process with substituted metal oxide and supported metal oxide (without any prior pretreatment). The long run stability test for Co-substituted CeO_2 was performed in a mixture of $CH_4/CO_2/N_2$ = 6/6/8, 20mL min^{-1}, (1 atm, GHSV = 12 000 mL g^{-1} h^{-1}) at 750 °C for 100 hours.

2.2.7 H_2-temperature programmed reduction. H_2-TPR studies employed a similar reactor to that used in the catalytic activity and connected with an online quadrupole mass spectrometer with an electron multiplier (Pfeiffer Vacuum, model Thermos star Omni GSD350). In this case, the catalyst weighed 100 mg and was processed at 150 °C for an hour in a nitrogen gas flow. After that, the same environment was used to bring the temperature down to room temperature. We do this preparation to get rid of any moisture and clean the surface. All of the catalysts were heated from room temperature to 800 °C at a steady heating rate of 10 °C min while being subjected to a 20 mL min^{-1} flow of H_2 (10%)/N_2.

2.2.8. Transient reaction studies. As was noted before, the transient reactions were conducted in a fixed bed reactor under comparable experimental circumstances. Before passing methane, Ar was introduced up to 100 °C to remove the moisture or any kind of adsorbed species over the samples. After this 100 vol% CH_4 was introduced into the reactor from room temperature to 800 °C at a rate of 20 mL min^{-1}. Pfeiffer Vacuum's Thermos star Omni GSD350 quadrupole mass with electron multiplier spectrometer was used to detect the products. After collecting the data up to 800 °C, the catalysts were cooled in an atmosphere of argon after heating the CH_4 from room temperature to 800 °C. After that, 20 mL min^{-1} of 100% CO_2 was introduced into the reactor while the temperature was raised from room temperature to 800 °C, and the reaction of the products was monitored.

2.3 Computational methods

Electronic structure calculations were performed using density functional theory (DFT) and were executed with the Quickstep[65] module provided by the CP2K program.[66] Exchange–correlation potentials were treated within the generalized gradient approximation (GGA) employing the Perdew–Burke–Ernzerhof (PBE) functional.[67] A double-valence plus polarization (DZVP) basis set, optimized according to the Mol-Opt method,[68] was implemented to expand the wavefunctions. For the auxiliary plane wave growth of the charge density, the energy cutoff was set at 500 Ry. Valence electrons have been represented directly, while core electrons have been addressed using norm-conserving Goedecker–Teter–Hutter (GTH) potentials.[81] The Brillouin zone was integrated using a reciprocal space mesh comprising just the gamma point. The DFT-D3 van der Waals corrections by Grimme[69] were applied to take into account the long-range dispersion forces.

The CeO_2 surface was simulated by the creation of a three-layered slab, oriented in the [−1 1 0] direction, with dimensions 21 Å × 23 Å, with 15 Å vacuum in the *z*-direction. The bottom layer was treated as a bulk layer and was held fixed in all optimization calculations. Atoms of the adsorbate and the top two layers of the slab were let to relax until the residual force on all atoms reached 4.5 × 10^{-4} a.u.

3 Results

3.1 Characterization of the catalysts

3.1.1 XRD analysis. Using XRD, the crystal structure of the catalysts has been investigated. Fig. 1a depicts the typical XRD

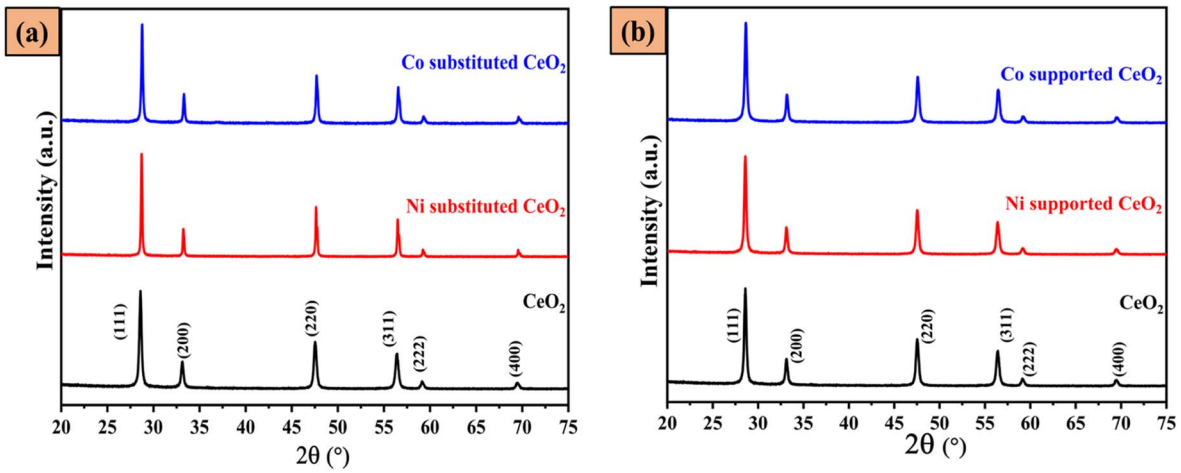

Fig. 1 (a) XRD patterns of CeO_2 and Ni- and Co-substituted CeO_2 samples and (b) XRD patterns of CeO_2 and Ni and Co supported over CeO_2 samples.

powder diffraction profile of the investigated samples, where the Bragg positions at 28.8°, 33.3°, 47.7°, and 56.6° correspond to the miller planes (111), (200), (220), and (311), respectively.[70] These planes are indexed to *Fm3m* space group CeO_2. No more peaks relating to Ni and Co could be observed within the sensitivity limit of the XRD equipment, indicating the possibility of Ni and Co substitution in the CeO_2 lattice. Additional evidence of the substitution is in the form of shifting of the XRD peaks in the substituted compound in comparison to only CeO_2. The replacement of Ce^{4+} (ionic radius = 0.87 Å) with Ni^{2+} (0.69 Å) and Co^{2+} (0.70 Å) ions caused a shift towards higher 2θ angles shown in Fig. S1.† Thus, a significant part of Ni and Co ions are substituted to form a solid solution. A complete substitution, however, cannot be assured and it is believed that the majority of the Co and Ni ions are in the substituted form, while a small concentration belonging to Ni/Co oxide may be present on the surface.

Rietveld refinement studies are shown in Fig. S2,† where analyses are compared with both observed and calculated fitting profile data. The structure refinement data reveal that CeO_2 with Ni and Co substitutions has a cubic structure with space group symmetry *Fm3m*.

Other refinement parameters are listed in Table S1† where a clear indication of a change in the lattice properties is observed. Considering the ionic sizes of substituent Co and Ni, the reduction in the lattice parameter is justified. Fig. 1b again shows a typical fluorite structure observed for all the supported catalysts and CeO_2. As observed from Fig. 1b, expected peaks of Ni (37.3°, 43.3° and 62.9°) and Co (45.0°, 65.5°) in the XRD of the supported catalyst are not noticeable in this case as well. This observation could be caused by a very fine dispersion of Ni and Co in the form of nanoparticles and these particles are small enough that XRD cannot detect them. Further XPS is performed to examine the chemical state of Ni and Co species over the surface of CeO_2 (as shown in the XPS analysis). Similar X-ray diffraction profiles for Ni-supported catalysts are also reported by Tang *et al.*[71] and Radlik *et al.*,[72] for whom reflections were noticeable only above 7 wt% and 10 wt%, respectively. Both values are higher than the 6.7 wt% utilized in this work.

We determined the actual content of Ni and Co in Ni and Co supported CeO_2 to be 4.9 wt% and 5.5 wt%, respectively, using the inductively coupled plasma optical emission spectroscopy (ICP-OES) analysis. In the case of Ni- and Co-substituted CeO_2, the content of Ni and Co was 6.2 wt% and 6.4 wt%, respectively. The BET surface area of Ni- and Co-substituted CeO_2 ranges between 3 and 5 $m^2\ g^{-1}$. These catalysts were prepared at high temperatures (~450 °C) causing a notable agglomeration and decreasing the surface area. The BET surface area of Ni, and Co supported CeO_2 is ~13 $m^2\ g^{-1}$.

3.1.2 Transmission electron microscopy (TEM). TEM analysis presents direct information regarding the particle size and *d*-spacing of catalysts. This *d*-spacing helps determine the lattice plane in the catalyst. Fig. S3† illustrates the HR-TEM image of the fresh catalysts. HR-TEM image analyses like particle size, *d*-spacing, and selected area electron diffraction (SAED) pattern of supported and substituted in CeO_2 catalysts are shown in Fig. 2. The HR-TEM images in Fig. S3a and b† illustrate the morphology and structure of Ni- and Co-supported CeO_2 which appear as spheres. It is apparent that catalysts are spongy spheres with an average particle size of 44 nm to 49 nm for Ni- and Co-supported CeO_2, respectively.

The hollow spheres can be seen clearly in Fig. S3a and b† which includes an excess of tiny particles with a mean size of 5–7 and 6–10 nm for Ni- and Co-supported CeO_2, respectively. This corresponds nicely with XRD pattern findings for Ni- and Co-supported CeO_2 and supported compounds indeed have Ni/Co nanoparticles over the CeO_2 surface. Consequently, HR-TEM shows that Ni- and Co-supported CeO_2 indeed have fine and uniform dispersion of Ni and Co nanoparticles, which are unnoticeable in XRD. The HR-TEM image of Ni and Co supported CeO_2 spherical crystallite reveals the dominant d (interplanar distance) = 0.312 nm and 0.32 nm, respectively clearly, which is ascribed to the (111) planes of CeO_2 crystals. The selected area electron diffraction

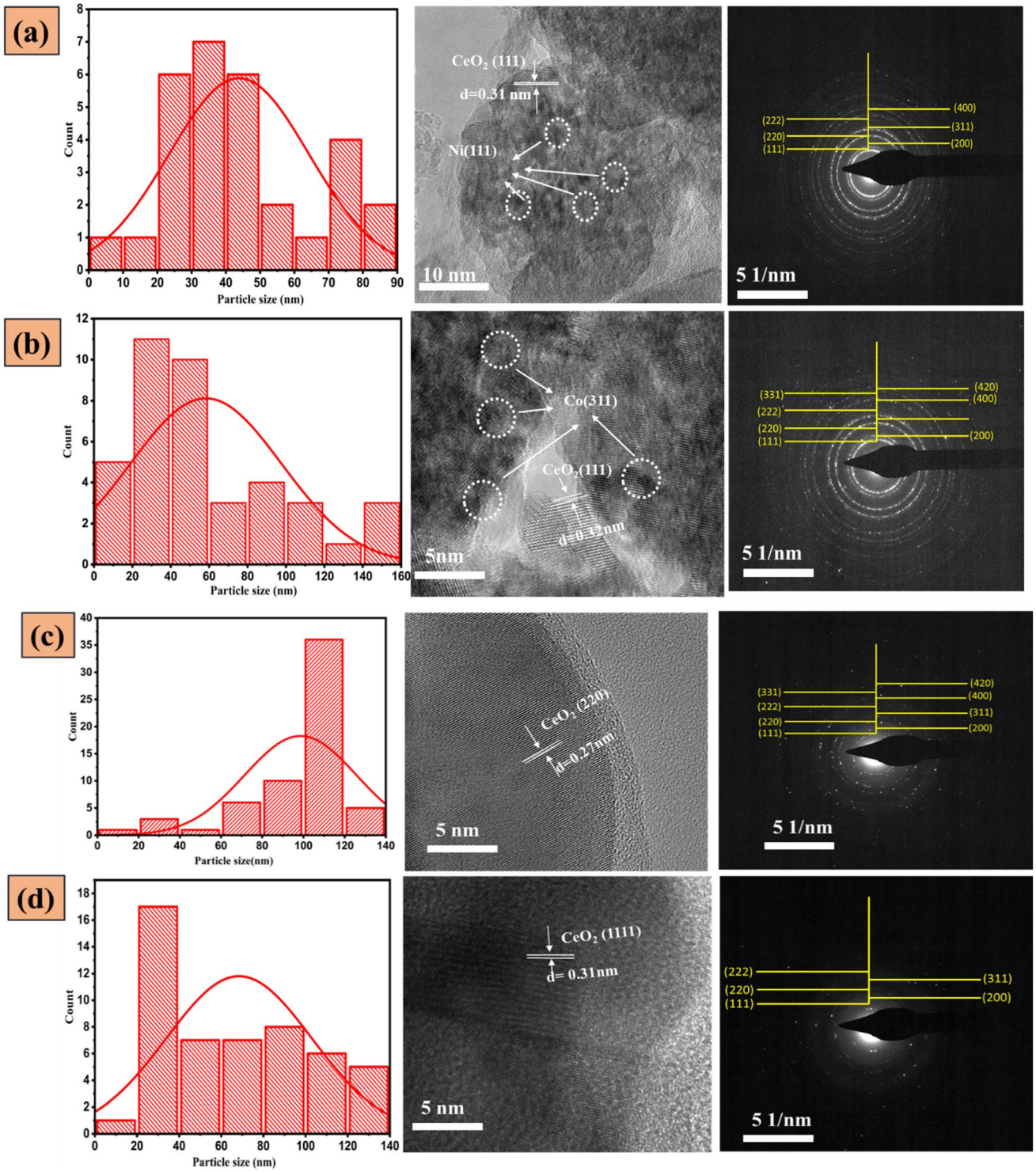

Fig. 2 HR-TEM analysis of (a) Ni supported over CeO_2, (b) Co supported over CeO_2, (c) Ni-substituted CeO_2, (d) Co-substituted CeO_2; particle size, *d*-spacing, and selected area electron diffraction (SAED) pattern.

patterns in Fig. 2a and b of the Ni- and Co-supported CeO_2 catalysts exhibit signals from (111), (220), (311), (400), (420) and (222) crystal planes in polycrystalline ceria. The presence of Ni and Co in TEM images by clear lattice fringe alignment is shown in Fig. 2a and b. One can clearly see both the Ni and Co on the surface of CeO_2 along with their *d* spacing value. The same has been marked in a dashed circle. Further, high-angle annular dark-field -scanning transmission electron microscopy (HAADF-STEM) and corresponding EDX elemental mapping revealed homogeneous elemental

distribution and the presence of Ni and Co supported over CeO_2 in Fig. S4a and b.† The HR-TEM images of Ni- and Co-substituted CeO_2 are given in Fig. S3c and d† which indicate agglomerated structures with distinguishable boundaries. Fig. 2c and d show the SAED pattern of Ni- and Co-substituted CeO_2, revealing polycrystalline fringes with an interplanar spacing distance equal to the lattice planes of the cubic CeO_2 crystal structure. The lattice fringes specify the crystalline nature of the synthesized sample. The calculated *d*-spacing values of 0.27 and 0.311 correspond to (200) and (111) planes of Ni- and Co-substituted CeO_2 respectively in Fig. 2c and d. No indication of the separated Co and Ni phases is obtained from the images which are in agreement. The average particle size of Ni- and Co-substituted CeO_2 was determined to be 68 and 100 nm, respectively. The greater particle size for substituted catalysts should contribute to the reduced BET surface area.

3.1.3 X-ray photoelectron spectroscopy (XPS). The chemical states and surface characterization of supported and substituted catalysts have been performed through X-ray photoelectron spectroscopy. The XPS analysis of fresh supported and substituted mono-metal in CeO_2 is represented in the form of the high-resolution XPS spectra of Ce 3d, Ni 2p, Co 2p, and O 1s. In the case of Ni supported over CeO_2, deconvoluted Ni $2p_{3/2}$ XPS denotes the peaks for two different chemical environments for nickel. The small peak at 852.4 eV (ref. 73) is consistent with the reference metallic Ni (852.4–852.6 eV)[74] and the other intense peak at ~853.9 eV is related to Ni^{2+} in NiO form.[75,76] The peaks at 858.3 eV and 861.4 eV (ref. 77) are the satellite peaks belonging to the metallic Ni and NiO, respectively (Fig. 3a). The percentage concentration of Ni^0 and Ni^{2+} is ~31% and ~69% respectively. Clearly, despite the attempt to disperse Ni metal nanoparticles, surface oxidation cannot be prevented which results in NiO formation. This is the reason that one sees NiO reduction in the H_2-TPR experiment (Fig. 4b). In the case of Ni-substituted CeO_2 no peaks related to the metallic Ni are observed. Two high-intensity peaks at 854.6 and 855.9 eV along with the satellite peaks at 858.1 eV and 861.6 eV (ref. 75, 76 and 78) are observed for Ni^{2+} and Ni^{2+}–OH, respectively (Fig. 3c).

In Co supported over CeO_2 Co $2p_{3/2}$ XPS exhibits binding energies at around 778.1 eV. Further, Co $2p_{3/2}$ is deconvoluted into three peaks at 777.5 eV, 779.4 eV, and 781.1 eV confirming that the Co was in 0, +2 and +3 oxidation states, respectively.[79,80]

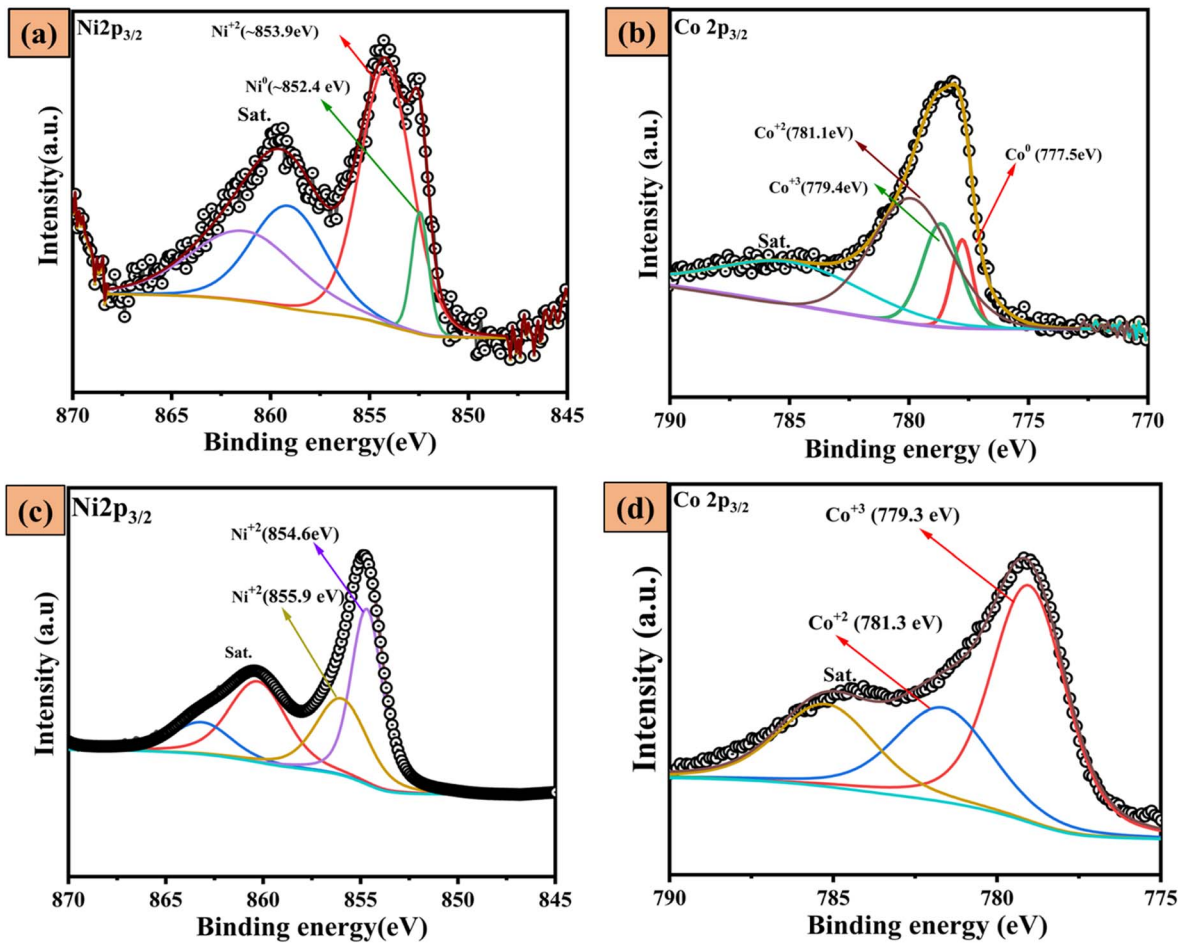

Fig. 3 XPS spectra of (a) Ni $2p_{3/2}$ in Ni supported over CeO_2, (b) Co $2p_{3/2}$ in Co supported over CeO_2, (c) Ni $2p_{3/2}$ in Ni-substituted CeO_2, and (d) Co $2p_{3/2}$ in Co-substituted CeO_2.

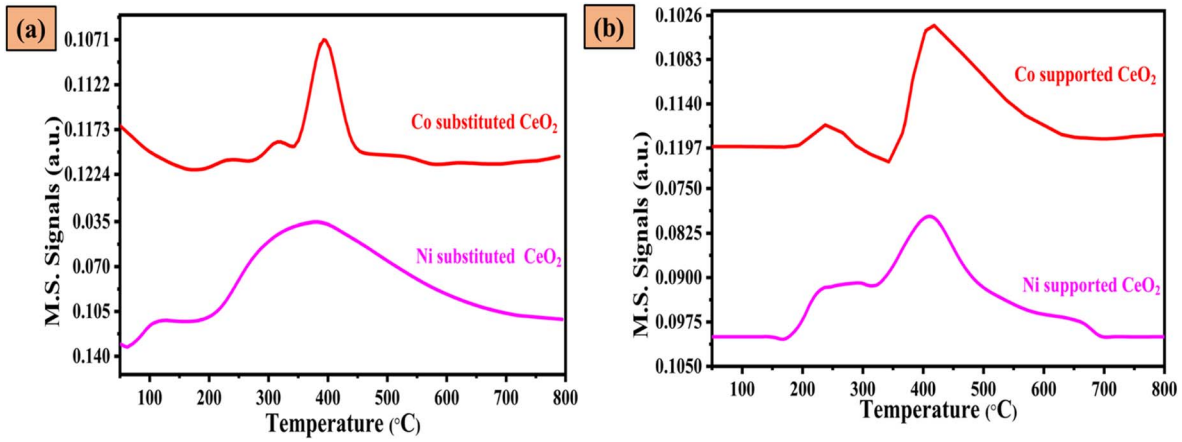

Fig. 4 H_2 temperature-programmed reduction profiles of Ni/Co substituted and supported over CeO_2 catalysts. Experimental conditions: 20 mL min^{-1} of 10% H_2 in N_2; temperature ramp rate is 10 °C min^{-1} from RT to 800 °C.

Co^{2+} is usually confirmed by the satellite peaks at 785.3 eV in the Co supported over CeO_2 catalyst (Fig. 3b).

The concentration of Co^0, Co^{2+} and Co^{3+} is ~17%, ~55% and ~28% respectively. The Co metal nanoparticles undergo oxidation. In the case of Co-substituted CeO_2, the Co 2p XPS demonstrates a broad peak for Co $2p_{3/2}$ at ~779.1 eV.[81] Further deconvolution results in two peaks at ~779.1 eV and 781.3 eV, which confirms that the Co was in +3 and +2 oxidation states respectively[82,83] (Fig. 3d). The presence of Co^{2+} in Co-substituted CeO_2 was further confirmed by the presence of a satellite peak at 785.2 eV. Atomic percentages of different oxidation states in substituted and supported catalysts are given in Table 1 below:

Thus, XPS is able to confirm the presence of Ni and Co both in supported and substituted compounds which was inconclusive from the XRD investigation.

High-resolution Ce 3d XPS spectra (Fig. S5†) and explanations are given in the ESI.† Also, Table S2† lists the binding energies (BE) and the area of each peak. XPS can provide valuable information in the form of the $Ce^{3+}/(Ce^{4+} + Ce^{3+})$ ratio based upon the surface concentrations. This ratio offers valuable information on the existence of surface defects, which play a vital role in determining the catalytic activity of ceria-based systems. Thus, the ratio of $Ce^{3+}/(Ce^{4+} + Ce^{3+})$ is estimated to illustrate the content of oxygen vacancies on the catalyst surface.[84] Table 2 presents the $Ce^{3+}/(Ce^{4+} + Ce^{3+})$ ratio for substituted and supported CeO_2, determined from XPS. As given in Table 2, we found that Co-substituted CeO_2 shows the highest fraction of Ce^{3+}. The occurrence of Ce^{3+} is related to oxygen vacancy formation. It is well known that vacancies and oxygen defects play a significant role in the dry reforming process, therefore an increase in defects is advantageous.[85] Oxygen vacancies may increase CO_2 adsorption and control the C–H activation on the catalyst surface[86] which is a critical stage in the dry reforming mechanism. Vacancies can also easily absorb and dissociate CO_2 into CO. Zhikun Peng et al.[86] have shown that a higher concentration of oxygen vacancies in the catalyst helps to remove the deposited carbon by the activation of CO_2 to create O_{ad}, which simultaneously eliminated the carbon deposition and maintained the high activity. Considering the highest number of defects in Co-substituted CeO_2, this catalyst is likely to show superior activity among other catalysts. High-resolution O1s XPS spectra are given in Fig. S6.† In Table 2, the content of oxygen vacancies around Ce^{3+} sites on the catalyst surface is illustrated by calculating the ratio of O″/O′ or chemisorbed oxygen to lattice oxygen from XPS spectra of O1s.

3.1.4 H_2-temperature programmed reduction (TPR). The reducibility of substituted and supported catalysts was studied by H_2 TPR. There has been a sincere effort in the literature in explaining the reducibility of similar catalytic systems. In general, the reducibility behavior has been explained based on the degree of metal oxide reduction. But our approach is to explain the reducibility in terms of reactive oxygen on the surface, especially in the substituted oxides. This approach appears more accurate as there is no need to distinguish if the reactive oxygen is from the substituted metal oxide or supported oxide and the contribution from both is taken into account. Additionally, in the substituted metal oxide systems such as Ni- and Co-substituted CeO_2, it is not wise to treat the substituted entity as the separated NiO_x and CoO_x phases. Contrastingly in

Table 1 Atomic percentage of different oxidation states of Ni and Co in substituted and supported catalysts

Samples	Ni-supported CeO_2		Co-supported CeO_2			Ni-substituted CeO_2	Co-substituted CeO_2	
Atomic%	Ni^0 ~31%	Ni^{2+} ~69%	Co^0 ~17%	Co^{2+} ~55%	Co^{3+} ~28%	Ni^{2+} 100%	Co^{2+} ~39%	Co^{3+} ~61%

Table 2 Ratio O″/O′ and the ratio $Ce^{3+}/Ce^{4+} + Ce^{3+}$ of supported and substituted catalysts

Samples	Ni-supported CeO_2	Co-supported CeO_2	Ni-substituted CeO_2	Co-substituted CeO_2
O″/O′	0.38	0.39	1.10	1.37
Fraction Ce^{3+} from Ce 3d $= \frac{Ce(III)}{Ce(IV) + Ce(III)}$	0.25	0.33	0.29	0.39

Ni- and Co-supported CeO_2 catalysts, separate NiO and CoO formation is possible, and their reduction behavior can be examined.

For the H_2-TPR of Ni-substituted CeO_2, reduction starts at around 50 °C and two broad peaks are observed at 124 °C and 318 °C (Fig. 4a). The peaks observed at low temperatures can be explained as being due to the reduction of oxygen adsorbed on the vacancies[87] caused by the incorporation of Ni^{2+} within the CeO_2. Thus, two forms of oxygen surface lattice exist and the one which is available at low temperature is generally useful in catalytic reactions. The broadness of the peaks suggests that the temperature required to reduce this oxygen varies in a broad range. It has been reported that the first peak is due to the reduction of surface species Ni^{2+} species on the CeO_2 surface and the second peak is due to strong Ni^{2+} substituted in CeO_2.[88] The larger area of the second peak suggests that the majority of the Ni exists in the substituted form. H_2-TPR of the Co-substituted CeO_2 catalyst (Fig. 4a) shows a significant signal even at 50 °C indicating that there are very weekly bonded lattice oxygen species available at temperature lower than 50 °C. Further, there are two minor peaks and one major peak at 247 °C, 320 °C and 498 °C in the TPR curves. In the literature, the two initial peaks are attributed to the two-step reduction ($Co_3O_4 \rightarrow$ CoO followed by CoO $\rightarrow Co^0$).[88] The third peak is probably due to substituted Co^{2+} which strongly interacts with the CeO_2. This peak is the most intense, confirming that the majority of Co^{2+} is in the substituted form. The peaks are comparatively sharper than those of Ni-substituted CeO_2, confirming the narrow and discrete energy ranges for surface oxygen in this catalyst.

The Ni-supported catalyst (Fig. 4b) shows 3 merged peaks with the most prominent one between 350 °C and 500 °C. Previous studies have shown that pure NiO without any support oxide involves two reduction peaks equivalent to the stepwise reduction of NiO: NiO $\rightarrow Ni^{\delta+} \rightarrow Ni^0$.[46] In our case, the reduction onset temperature starts at 200 °C and flattens at 260 °C which can be ascribed to NiO reduction to $Ni^{\delta+}$. Thus, the surface Ni nanoparticles invariably produce NiO species in the open atmosphere. The prominent peak at 440 °C for Ni-supported CeO_2 may be due to the reduction of some ($Ni^{\delta+} \rightarrow Ni^0$).[89] The high-temperature peak is more prominent which explains that the compound may have significant $Ni^{\delta+}$ species apart from NiO.

Co supported over CeO_2 shows two prominent (Fig. 4b) peaks in the ranges of 190–284 °C and 345–550 °C. Here also, surface oxidation of Co nanoparticles is expected which gives rise to CoO_x species. The reduction of Co_3O_4 starts at 180 °C and happens as a two-step reduction; $Co_3O_4 \rightarrow$ CoO $\rightarrow Co^0$.[90,91] While the shoulder observed at 244 °C for Co supported over CeO_2 was ascribed to the reduction of $Co_3O_4 \rightarrow$ CoO, the prominent peak seen at 450 °C for Co supported over CeO_2 was attributed to the reduction of CoO $\rightarrow Co^0$.[91] Sharp negative peaks at 300–400 °C indicate the hydrogen spill over phenomena that happened as a result of the dissolution of hydrogen over this sample, which might be due to the presence of Co atoms. It may also be caused by the production of hydrogen as a consequence of hydride breakdown. The TPR behavior of PdO/ZrO_2, PdO/CeO_2, and $PdO/Al2O_3$ was also observed by several researchers.[92–94] Clearly, the reduction behavior including peak shape and temperature changes substantially after the substitution and both the substituted compounds show significantly lower reduction onset. Quantitively, the reducibility (amount of hydrogen per weight of the catalyst) for Ni-supported CeO_2 and Co-supported CeO_2 is ~2.4 mmol g^{-1} and 4.8 mmol g^{-1} respectively.

The reducibility of Ni-substituted CeO_2, and Co-substituted CeO_2 is ~3.1 mmol g^{-1} and ~5.4 mmol g^{-1} respectively. Co-substituted CeO_2 shows the highest reducibility among other catalysts and also it has significant reducibility at the lowest temperature among all the catalysts. This may be helpful in dry reforming reactions given that the first step in the reaction is methane decomposition which deposits carbon on the surface. This deposited carbon is oxidized in the second step which needs lattice oxygen participation. Thus, the availability of lattice oxygen at low temperature is crucial.

4 Catalytic activity

4.1 Dry reforming reaction activity test

The catalytic activity of dry reforming of methane is expressed in the conversion of reactants as a function of temperature (Fig. 5a and b). Monometallic Ni-supported catalysts showed a significant methane conversion (98%) at 650 °C and above, proving excellent activity for methane activation. In contrast, Co-supported catalysts showed methane conversion of about 81% at 650 °C. In terms of CO_2 conversion (Fig. 5b), Co-supported CeO_2 exhibited 90% CO_2 conversion compared to Ni-supported CeO_2 (84.3%), but a higher temperature (800 °C) is required to attain it. Conversion of CO_2 saturates at 84% in the case of Ni/CeO_2 at 700 °C and does not change even after raising the temperature to 800 °C.

In the case of the substituted system, the Ni-substituted catalyst initially shows a very high conversion but within 40

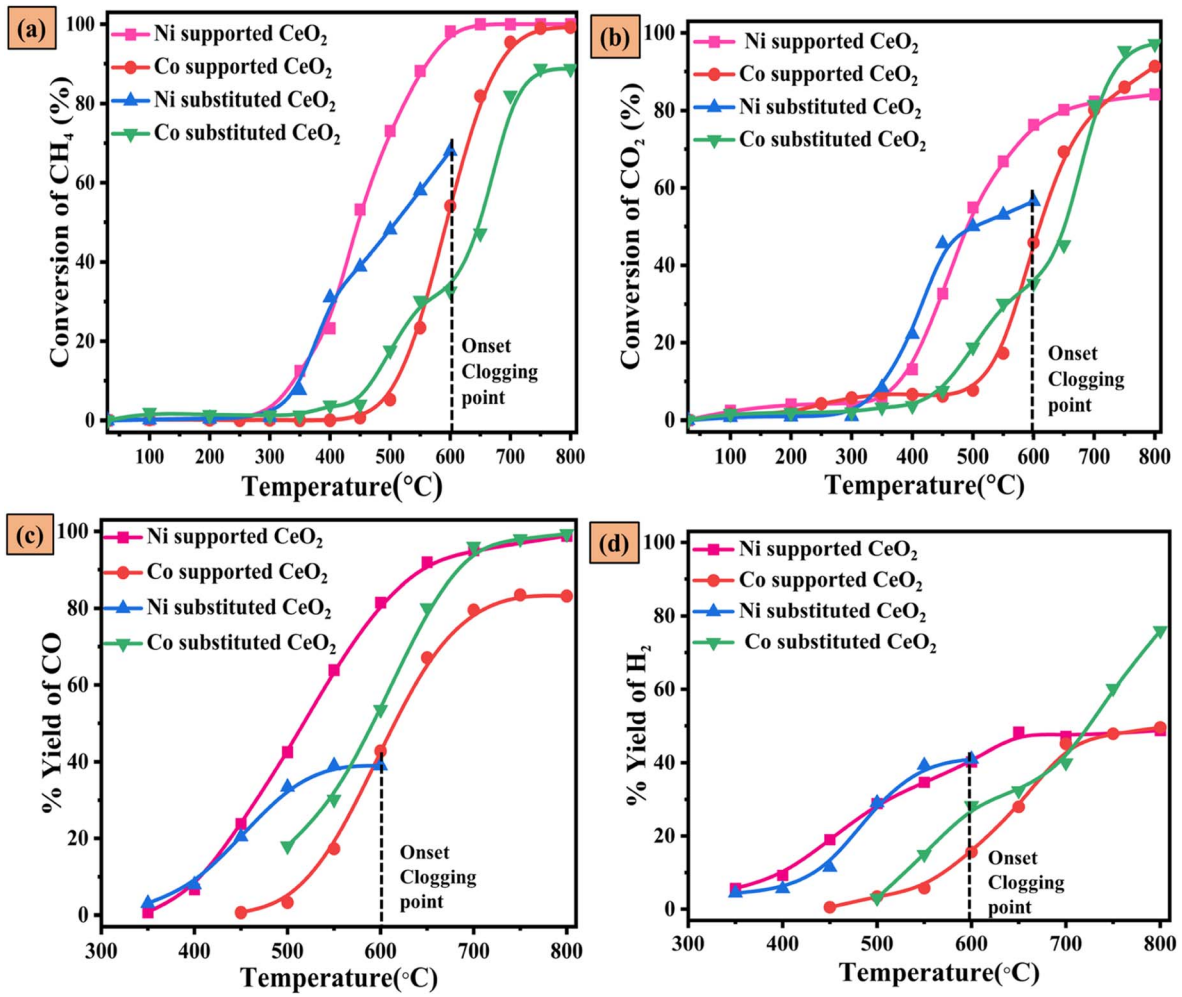

Fig. 5 Catalytic activity for the dry reforming of methane: (a) CH_4 conversion, (b) CO_2 conversion, (c) CO yield, and (d) H_2 yield as a function of temperature. Reaction conditions: room temperature to 800 °C, 1 atm, $CH_4/CO_2/N_2 = 1/1/18$, flow rate = 20 mL min^{-1} and GHSV = ~12 000 mL g^{-1} h^{-1}.

minutes clogging occurs, and at 600 °C flow rates of the reactants completely stop. The CH_4 and CO_2 conversion could not be calculated after the clogging onset. But in the case of the Co-substituted catalyst a very good CO_2 and CH_4 conversion has been observed although the conversion temperatures are inferior to those of Ni-supported CeO_2. In terms of methane conversion, Co-supported CeO_2 has better activity than Co-substituted CeO_2, particularly above 550 °C. In contrast, Co-substituted CeO_2 has some exclusivity for CO_2 conversion and a maximum conversion (92.5%) at 700 °C and above is obtained over this catalyst. This is the highest CO_2 conversion among all the studied catalysts. As shown in Fig. 5a and b, Co-substituted CeO_2 exhibited 97% CO_2 conversion and 90.8% CH_4 conversion when the reaction temperature reaches 800 °C.

The yield of CO and H_2 is given in Fig. 5c and d and it is clear that all the supported catalysts show higher CO yield than H_2 due to the reverse water–gas shift reaction (RWGS) ($CO_2 + H_2 \rightarrow CO + H_2O$ $\Delta H^0 = 41.1$ kJ mol^{-1}). The formation of H_2O is evident in the outlet gas stream where the moisture trap was attached. RWGS is a usual side reaction that happened during the DRM reaction and due to which the H_2/CO ratio at 800 °C for Ni and Co supported CeO_2 is 0.48 and 0.61, respectively. This ratio deviates from the theoretical ratio of unity. H_2/CO for Co-substituted CeO_2 is 0.8 at 800 °C which is more than that of the supported catalysts confirming that the occurrence of the side reactions is less prominent in comparison to the supported catalysts.

The Ni particle size has an effect on the reactivity of the DRM reaction. In various studies, it is reported that if the particle size of Ni ranges between 1.0 nm and 2.8 nm (ref. 95 and 96) it would be good for DRM. In some cases, it is found that if the Ni particle size is 22 nm it is good for coke resistance during the DRM.[50] Other factors such as the participation of lattice oxygen in the removal of coke are also important as shown by Efstathiou *et al.*[50] In our case, in Ni-supported CeO_2, the particle size of Ni is around 5–7 nm that could be the reason for higher methane conversion which further led the higher carbon deposition over the catalyst as supported by the TGA. The same explanation is also given for Co-supported CeO_2. The catalytic activity of Co-substituted CeO_2 is also superior to both Ni- and

Co-supported CeO_2 in terms of H_2 and CO production at 800 °C (Fig. 5c and d). We have also compared the catalytic activity of Co-substituted CeO_2 with existing Co-based DRM catalysts as shown in Table S5.† So, the good catalytic activity of Co-substituted CeO_2 can be explained in the light of H_2-TPR (see Fig. 4a) and XPS results where it has been shown that this catalyst is highly reducible in nature (easily accessible lattice oxygen) and contains the largest concentration of oxygen defects (see Table 2).

4.2 Activity under isothermal conditions

The dependency of catalytic activity on time was studied at a constant temperature of 800 °C (isothermal) for 300 minutes on the same sample previously used in the catalytic activity test (Fig. 6). Both cobalt-supported and substituted catalysts exhibit a stable response during 300 minutes on stream. At the end of 300 min, CH_4 conversion decreases by only 4–6% while CO_2 conversion decreases only by 5–7% on cobalt-based catalysts (Fig. 6a and b). Ni-supported CeO_2 shows a prominent decrease in the conversion within 5 hours. Here, CH_4 conversion decreases by 15% and CO_2 conversion decreases by 12% (Fig. 6a and b). Since the CO yield was higher than the H_2 yield (Fig. S8†), the H_2/CO ratio is lower than 1.0 for all the catalysts.

Co-substituted CeO_2 shows the highest H_2/CO ratio (~0.8) making it an important DRM catalyst (Fig. 6c) and corroborating our claim based on H_2-TPR and XPS. In the entire isothermal studies, the Co-substituted CeO_2 system demonstrated methane conversion values close to the thermodynamic equilibrium value. In the case of Ni- and Co-supported catalysts, the CH_4 conversion was lower than the thermodynamic equilibrium conversion at 800 °C. Thermodynamic H_2/CO was higher than experimental H_2/CO for all the catalysts.[97] This behavior is believed to be due to the occurrence of the reverse water-gas shift reaction ($CO_2 + H_2 \rightarrow CO + H_2O$ ΔH^o = 41.1 kJ mol^{-1}) which is preferred at high temperatures due to its endothermic nature.

Fig. S9† presents the results of the 100 hour test conducted at 700 °C in the mixture $CH_4/CO_2/N_2 = 6/6/8$ and the flow rate = 20 mL min^{-1}, GHSV = ~12000 mL g^{-1} h^{-1} and TGA of the spent catalyst after 100 hours for Co-substituted CeO_2. Co-substituted CeO_2 exhibited stable CH_4 conversions and only 3.7% deactivation of methane over 100 hours of time on-stream (TOS) was

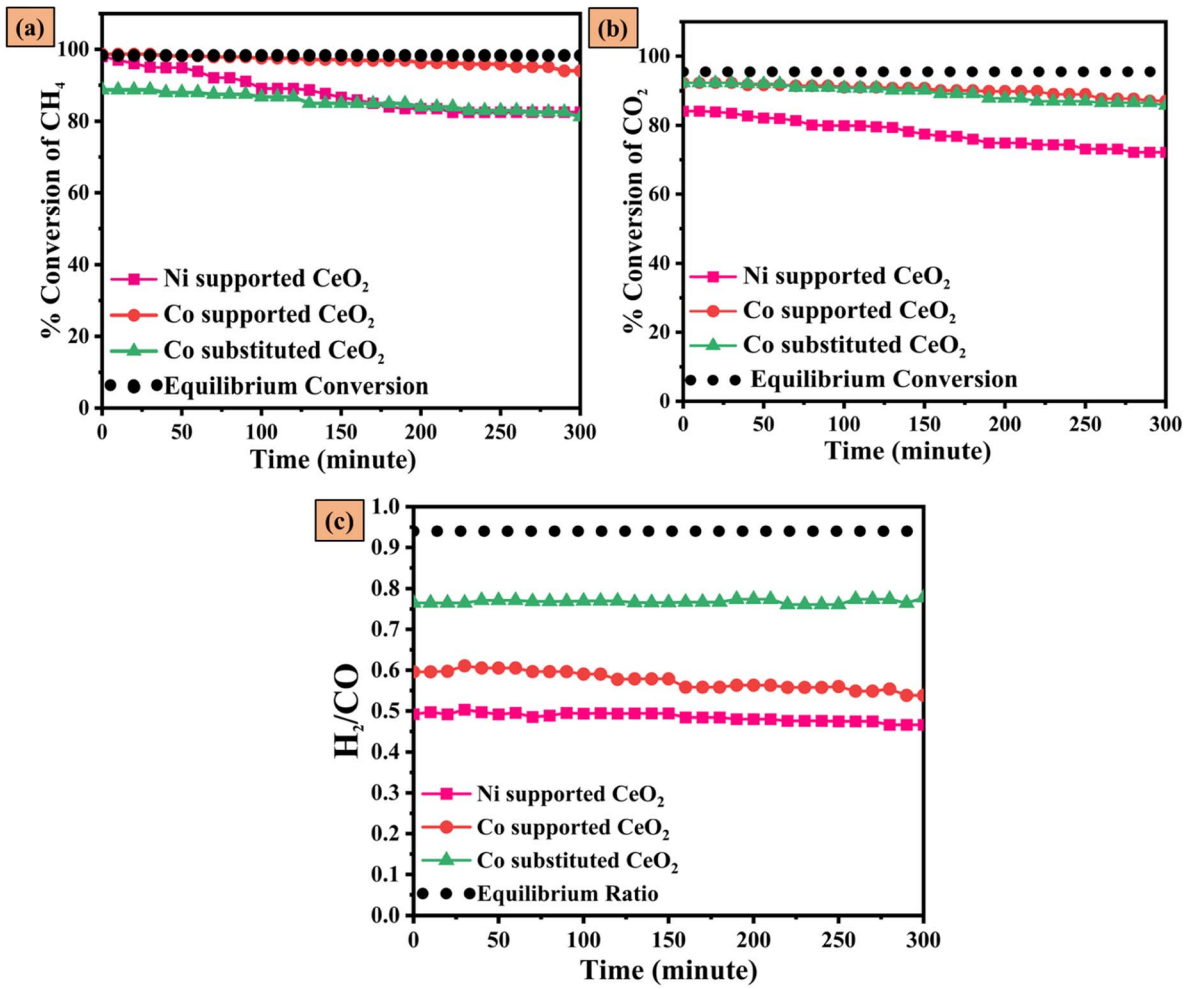

Fig. 6 Catalytic activity for the dry reforming of methane: (a) CH_4 conversion, (b) CO_2 conversion as a function of temperature and (c) H_2/CO. Reaction conditions: 800 °C, 1 atm, $CH_4/CO_2/N_2$ = 1/1/18, flow rate = 20 mL min^{-1} and GHSV = 12 000 mL g^{-1} h^{-1}.

observed. This conversion behavior over time was closely related to the literature in the Table S6.† Table S6† presents the comparison of the feed concentration of reactants (CH_4/CO_2), reaction temperature, time on steam (TOS) and the amount of deposited carbon after reaction by the TGA for the different Ni and Co catalysts for DRM. Clearly, Co-substituted CeO_2 is among the best carbon-resistant catalysts after 100 hours of the DRM reaction.

5 Post-characterization of the catalysts after the isothermal activity test

5.1 Thermogravimetric analysis (TGA) and derivative of thermogravimetric (DTG) analysis

TGA/DTG analysis of the substituted and supported catalyst was performed to evaluate the deposited carbon over the catalyst during the dry reforming reaction. Carbon deposition is expected during the DRM reaction.

The weight losses resulting from the combustion of the carbon deposited on the consumed catalysts are shown in Fig. 7. Clearly, the Ni supported over CeO_2 catalyst showed more weight loss than Co-supported CeO_2. The prominent weight loss (~19.8%) in the spent Ni-supported CeO_2 is noticed at the onset temperature of 458 °C. In contrast, significantly lesser (~2.5%) weight loss in the spent Co-supported CeO_2 is noticed at the onset temperature of 483 °C. Thus, the stability of Co-supported CeO_2 against carbon deposition is clear. It is well documented in the literature that DRM happens *via* a two-step process where methane decomposition occurs first to produce hydrogen and carbon, and in the second step the produced carbon gets oxidized to CO_2.[98–101] Thus, higher accumulation of carbon is an indication of the more prominent methane decomposition reaction and less prominent carbon oxidation reaction. Not only Co supported but Co-substituted CeO_2 also shows very low carbon accumulation (2.3%). This shows that both CH_4 decomposition and carbon oxidation are prominent reactions in cobalt-based catalysts. This also relates well with the catalytic activity test (Fig. 5) where Ni-supported catalysts have shown the highest methane conversion but lower CO_2 conversion in comparison to cobalt-supported and substituted catalysts.

The consumed monometal catalysts' derivative weight loss analysis (DTG) was plotted to distinguish the different types of carbon deposited during the reaction in Fig. 7b. One characteristic peak was detected for Ni supported over CeO_2, representing the formation of only one kind of carbon formation, which can be oxidized at around 478 °C. In the same way, Ni-substituted CeO_2 also shows only one kind of carbon, oxidizable at around 487 °C. Instead, Co supported over CeO_2 exhibited two peaks indicating two different types of carbon formation; the first type is oxidized at around 247 °C, and the second type is oxidized at around 370 °C. Co substituted over CeO_2 exhibits a single peak at around 775 °C. Thus, both substituted and supported catalysts behave differently in terms of deposited carbon type. It is usually acknowledged that amorphous carbon oxidizes at lower temperatures followed by other types of carbons.[102]

5.2 TEM analysis of the spent catalysts

Fig. S10† shows the TEM images of all the spent catalysts. No carbon filaments are detected in the TEM images of Co supported over CeO_2 and Co-substituted CeO_2 in agreement with TGA. Only a small amount of amorphous carbon layers was observed in TEM. In contrast, Ni supported over CeO_2 and Ni-substituted CeO_2 catalysts reveal high carbon formation, with many carbon filaments after the DRM reaction (Fig. S10a and S†10c). The diameter of filaments was ~11 nm, and ~45 nm for Ni supported over CeO_2, and Ni-substituted CeO_2, respectively. After the DRM reaction, the particle size increases significantly, indicating thermal sintering and carbon coating. In the case of Ni-substituted CeO_2, the particle size increases to almost twice of the fresh catalyst. This was the likely reason for blocking that happened during the reaction. The particle size for spent Co supported over CeO_2 and spent Co-substituted CeO_2 catalysts

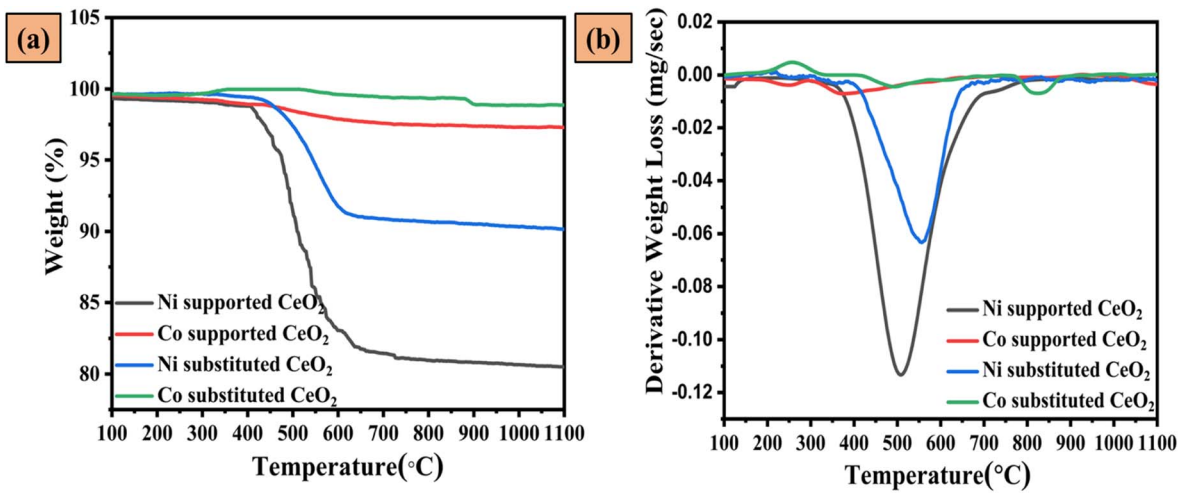

Fig. 7 TGA curves and derivative weight losses in an air atmosphere after being used in the reaction at 800 °C for 5 h isothermal studies.

was found to be ~62 nm and ~79 nm, respectively, which is also larger in comparison to the fresh catalysts.

6 Transient CH_4 and CO_2 responses

To understand the carbon deposition and its oxidation behavior, transient reaction analysis is carried out on an online mass spectrometer. First, the activity of methane in the absence of CO_2 is tested over all the catalysts. Fig. 8 shows the response of methane conversion in terms of H_2, CO, and CO_2 formation from RT to 800 °C. The Ni-substituted catalyst shows the highest H_2 production compared to any other substituted and supported catalyst (Fig. 8a); therefore, it has the highest methane decomposition activity which peaks at 550 °C. Further, a low amount of CO (Fig. 8b) and CO_2 (Fig. 8c) formation over this catalyst justifies that the oxidation products due to the reaction between methane and lattice oxygen are not forming efficiently. Noticeably, the production of hydrogen, CO, and CO_2 occurs at the same temperature of ~350 °C, justifying that methane decomposition and its partial oxidation are occurring together. Thus, it can be stated that while the surface of the Ni-substituted catalyst is active for methane decomposition to hydrogen, it is not very active for its partial oxidation. In other words, lattice oxygen participation is not significant. This relates well with the conversion curves where onset clogging occurred in the Ni-substituted CeO_2 due to high carbon decomposition *via* the methane decomposition reaction ($CH_4 \rightarrow C + 2H_2$).

In the case of Co-substituted CeO_2, lower H_2 production is noticed as compared to Ni-substituted CeO_2. Further, it showed a significantly higher amount of both CO (between 550 and 700 °C) and CO_2 (between 400 and 530 °C) confirming that Co substituted CeO_2 is a good catalyst for methane partial oxidation. This again relates well with the catalytic activity seen earlier where this catalyst has shown high CO_2 conversion and much less carbon decomposition. Interestingly, the formation of CO_2 starts even before H_2 production (notice the minor peak between 400 and 450 °C) confirming the independent participation of lattice oxygen. Another interesting feature is the very sharp nature of CO and CO_2 production at around 500 °C which infers swift product formation. It is worth noting that H_2-TPR also shows a sharp reduction peak in the same temperature range. Clearly, lattice oxygen is very reactive and easy to remove within this temperature range which reacts with methane to

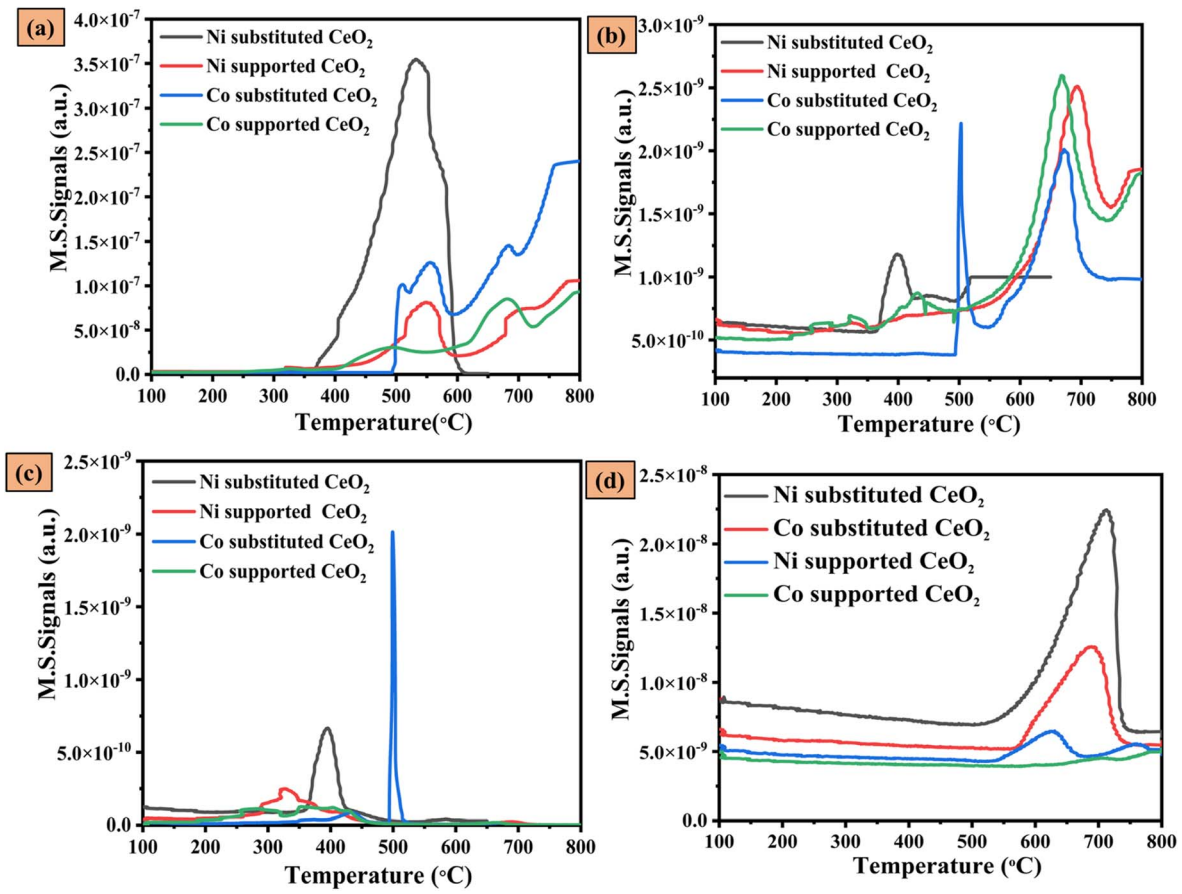

Fig. 8 CH_4 conversion: (a) H_2 response during CH_4-TPSR, (b) CO response during CH_4-TPSR, (c) CO_2 response during the CH_4 decomposition test over Ni, Co-substituted and supported CeO_2. Ni-substituted CeO_2 blocked abruptly at 650 °C after passing only CH_4. (d) Temperature-programmed reaction (TPRn) with CO_2 profiles of CO after the exposure to CH_4 over the catalysts from room temperature to 800 °C; coke was converted into CO over Ni, Co-substituted and supported CeO_2.

form CO and CO_2. While CO_2 formation stops swiftly, CO continues to form and forms another broad peak between 550 and 700 °C. This peak probably forms due to the deposited carbon reacting with another type of oxygen on the surface. The formation of a higher amount of CO than CO_2 is indicative of the larger contribution of partial oxidation than complete methane combustion.

Both Ni- and Co-supported CeO_2 behave almost similarly except that the former shows slightly higher H_2 formation. Ni- and Co-supported CeO_2 show a good amount of CO production which is comparable to Co-substituted CeO_2. So, lattice oxygen in both the supported catalysts precipitates and reacts with methane unlike Ni-substituted CeO_2. Negligible CO_2 is detected on both the supported catalysts unlike Co-substituted catalysts confirming a minor contribution of the methane combustion reaction. Similar reactivity of both the catalysts suggests that metal–support interactions are not prominent in the supported catalysts. The formation of oxidation products such as CO and CO_2 in the supported catalysts can be ascribed to the direct interaction between methane and the lattice oxygen of ceria or free metal oxide on the CeO_2 surface.[48,49,51,52,103,104]

TGA was used to verify the carbon deposition trend over the catalyst after methane decomposition. The obtained profiles in Fig. S11† are in perfect agreement with the results discussed

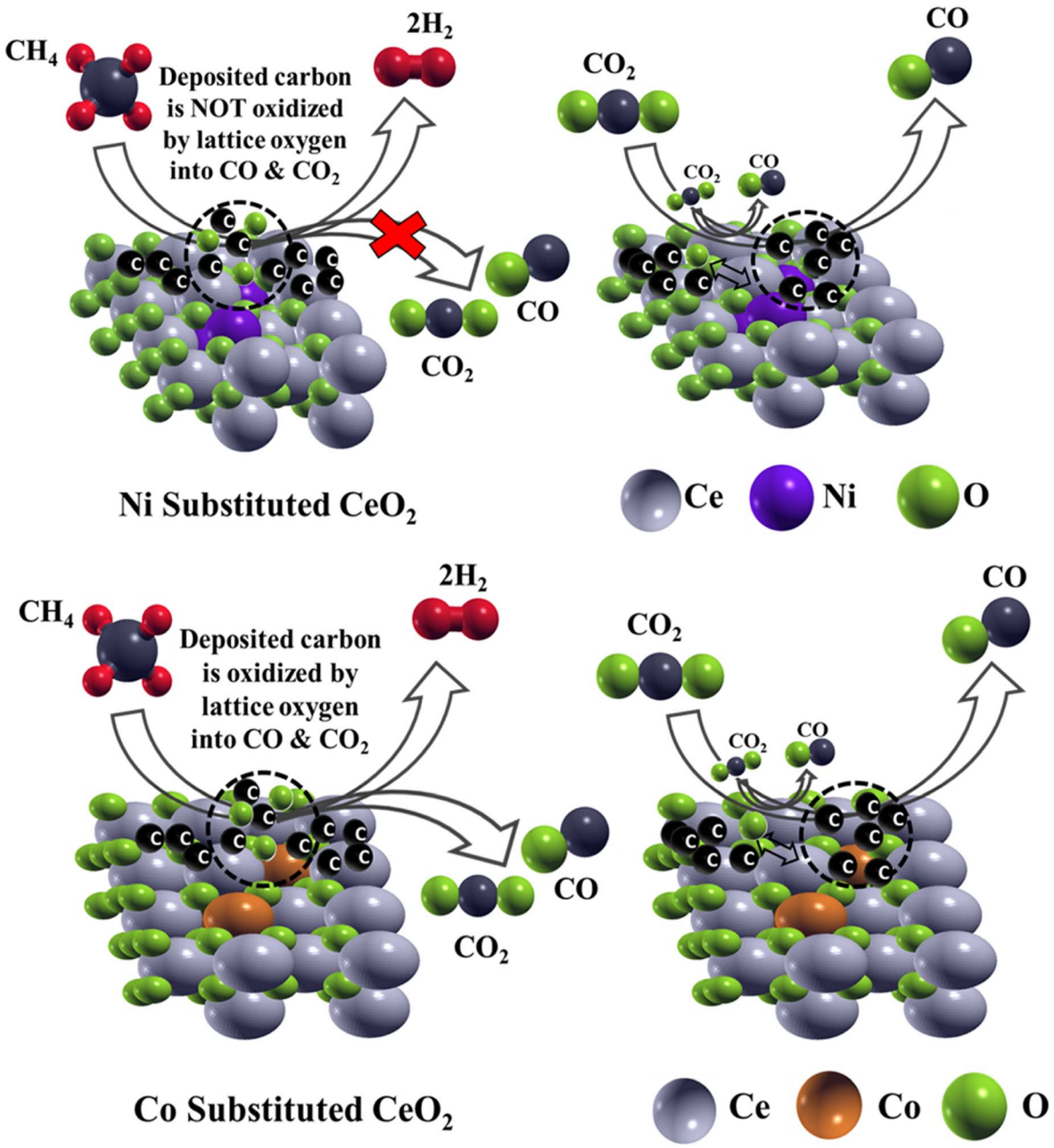

Scheme 1 Sketch for the mechanism on the basis of transient studies of methane decomposition and the CO_2 reaction with deposited carbon after CH_4 decomposition on Ni- and Co-substituted CeO_2.

above in Fig. 8. Ni-substituted CeO_2 shows the highest weight loss of ~14% which is in accordance with the extensive methane decomposition. Ni-supported CeO_2 catalysts show a weight loss of ~7.5% which is also higher than that of both Co-substituted and supported CeO_2. Both the cobalt-based catalysts show almost the same weight loss of ~4%. The results are in accordance with the transient methane reaction.

To understand the role of CO_2 in the removal of deposited carbon once again methane is reacted in a similar experimental setup. This is followed by the reaction with CO_2 in the same manner (Fig. 8d). It is expected that CO_2 will oxidize the deposited carbon and convert it to CO. Due to the clogging of Ni-substituted CeO_2, the reactor tube was opened and repacked. To maintain the uniformity, the same step was done for all the catalysts. The Ni-substituted CeO_2 catalyst is found to show the highest CO production during the reaction with CO_2 followed by the Co-substituted CeO_2 catalyst although it was expected that the Co-substituted catalyst would show the highest CO production due to its superior activity towards CO_2 (see Fig. 5). Therefore, higher carbon loading is probably the reason why the Ni-substituted catalyst is showing the highest CO production. Evidently, CO_2 is a good oxidant to remove the deposited carbon. Supported catalysts show minimal CO production in reaction with CO_2 which follows the TGA trend shown in Fig. 8d. It is worth remembering that both the supported catalysts have shown large CO production during the methane transient test (Fig. 8b). So, the source of CO production in the case of Ni- and Co-supported catalysts is also the oxidation of methane *via* lattice oxygen and not just the oxidation of deposited carbon. It is intriguing when all the active sites are blocked, how is CO_2 able to adsorb and oxidize the deposited coke. A basic and simplistic reason is the amorphous nature of carbon which has a highly porous nature allowing the CO_2 to access the active sites beneath it.

Based on transient experiments, the most acceptable pathway on Ni-substituted CeO_2 involves methane decomposition to generate H_2 and adsorbed carbon. The carbon on the catalyst reacts further with CO_2 to produce CO as suggested by Mark *et al.*[105] On Co substituted CeO_2, an additional pathway involving methane partial oxidation may happen because lattice oxygen is actively involved as shown in Scheme 1. Thus, a bi-reforming type of process is happening on this catalyst. It is difficult to point out the contribution of the two processes. Both Ni- and Co-supported catalysts follow similar pathways. Here both methane decomposition and partial oxidation contribute significantly and the carbon oxidation using CO_2 is negligible as shown in Fig. S12.†

7 *Ab initio* calculations of substituted catalysts

First principal computations were performed on the Ni and Co substituted CeO_2 catalyst surface to investigate the contribution of substituents. The catalyst surface was generated by creating a three-layer slab of CeO_2, oriented [−1 0 1], with periodicity intact in the *x* and *y* directions, while adding a region of vacuum in the *z* direction. The surface was optimized, following which Ni or Co was substituted in place of a Ce atom in two surface layers, as shown in Fig. 9. The bottom layer was left as pure ceria, to mimic the bulk. The substituted structure was optimized, with the bulk layer kept rigid. Fig. 9a and b shows the resulting optimized structure for Ni-substituted and Co-substituted CeO_2, respectively. It is apparent that the relaxed structure of the Co-substituted surface has oxygen atoms positioned outwards relative to surface Ce atoms, while that of the Ni-substituted surface has O atoms positioned inward relative to surface Ce atoms. This indicates that O atoms are readily available for reaction in the Co-substituted surface while availability is hindered in the Ni substituted surface.

To further study the consequence of the positions of oxygen atoms on catalytic action, adsorption of methane on the surface was studied. The methane molecule was positioned on three different sites on both surfaces as shown in Fig. S13,† in proximity to a surface Ce atom, a surface Ni or Co atom, or a site intermediate to Ce and substituent positions. The entire system was optimized, with the bottom layer of the slab maintained fixed. Adsorption energy was then computed as the difference between the sum of the individual energy of a slab and a methane molecule, and the energy of the relaxed methane-slab system. For Ni-substituted CeO_2, it was found that the adsorption energy at the intermediate site was the lowest at 8.053 kcal mol^{-1}, as compared to 15.028 kcal mol^{-1} at the Ni site and 17.543 kcal mol^{-1} at the Ce site. For Co-substituted CeO_2, the Co site and intermediate site are found to have a similar energy, with that of the Co site at 46.988 kcal mol^{-1} being slightly lower than 47.405 kcal mol^{-1} at the intermediate site, and both lower than 54.984 kcal mol^{-1} at Ce site. While adsorption is found to be most favorable at an intermediate site in the Ni-substituted catalyst and the Co site in Co-substituted catalyst, we note that the site preference is not strong.

To confirm the difference in the availability of oxygen for reaction with methane brought about by different substituents Co or Ni, the creation of oxygen vacancies was studied for both cases. In both structures, the slab is modified by removing an oxygen atom. As the site preference is not found to be significant, oxygen atoms from different positions are removed. For both catalysts, an oxygen vacancy is created either at a position in the neighborhood of the substituted atom or in the vicinity of the Ce atom. The energy of the catalyst with oxygen vacancies (E_{VS}) and half of a relaxed oxygen molecule ($E_{\frac{1}{2}O_2}$) is subtracted from the intact catalyst without vacancies (E_{Slab}), to estimate the energy of vacancy formation ($E_{Vacancy}$) as explained by eqn (1).

$$E_{Vacancy} = E_{VS} + E_{\frac{1}{2}O_2} - E_{Slab} \quad (1)$$

The vacancy formation energy for all cases is summarized in Table 3. In the case of Ni-substituted CeO_2, the energy for oxygen vacancy creation in proximity to Ni is 48.097 kcal mol^{-1} while it is 35.054 kcal mol^{-1} in proximity to Ce, indicating that the presence of Ni hinders the removal of the oxygen atom for reaction. Further, the energy of vacancy formation in Co-substituted CeO_2 is significantly lower regardless of the position of the oxygen atom removed. The energy for the removal of oxygen atom near Co is −37.870 kcal mol^{-1} while it is

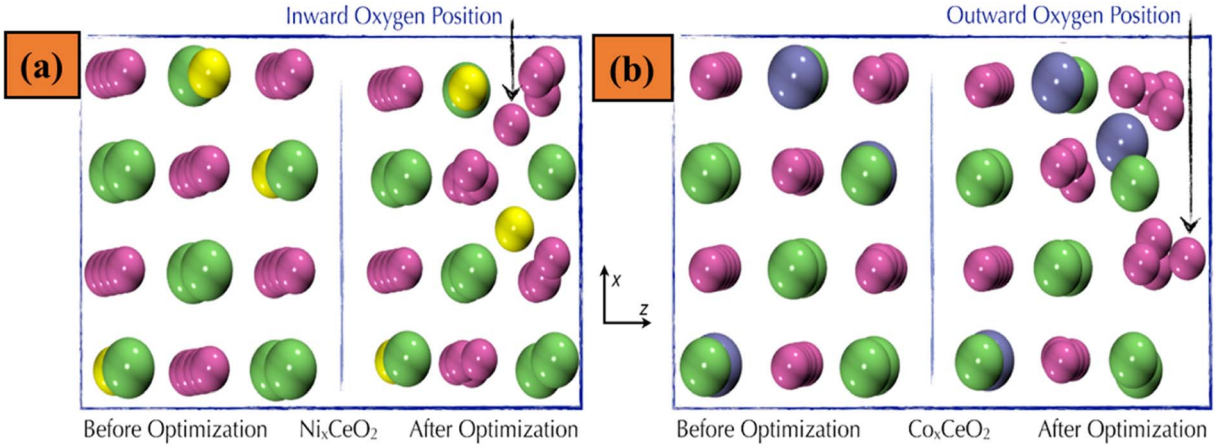

Fig. 9 Relaxed slab of CeO_2 substituted with (a) Ni and (b) Co has significantly different positions of surface oxygen atoms. As indicated by the arrows, surface oxygen tends to move outward from the surface in the presence of Co while it moves inwards in the presence of Ni. Color code: Ce – green; O – pink; Ni – yellow; and Co – ice blue.

Table 3 Vacancy formation energy for Ni- or Co-substituted CeO_2

Contents	Ni-substituted CeO_2		Co-substituted CeO_2	
Atom nearest to an oxygen vacancy	Ni	Ce	Co	Ce
Energy of vacancy formation (kcal mol^{-1})	48.097	35.054	5.812	−37.870

5.812 kcal mol^{-1} for the removal of oxygen atom near Ce. This shows that the presence of Co in the catalyst encourages the removal of oxygen from the catalyst. The vacancy energy confirms that the availability of surface oxygen for the oxidation of methane is significantly higher for Co-substituted CeO_2 as compared to Ni-substituted CeO_2, thus influencing the progress of reaction and consequently the effectivity of catalysts.

We also performed DFT calculations to evaluate CO_2 adsorption energies on Ni- and Co-substituted CeO_2. Similar to CH_4 adsorption, these calculations were performed considering multiple sites. Our results revealed that the Co-substituted system absorbs CO_2 much better than the Ni counterpart. The adsorption energies in Co- and Ni-substituted systems are −68 and −3.6 kcal mol^{-1}.

8 Apparent activation energy estimation for Co-substituted CeO_2

Considering the fact that Co-substituted CeO_2 has the desired activity, stability, and right CO/H_2 ratio, its kinetic parameters, and apparent activation energies are estimated. For this, CH_4 and CO_2 conversion are studied at different flow rates (as shown in Fig. S14†). Fig. S15a† presents the plots of CH_4 conversion as a function of temperature and space-time (W/F), which gives the methane conversion rate (R_{CH_4}). The methane conversion rate (R_{CH4}) increased as the temperature changes from 723 K to 798 K, as shown in Fig. S15b.† The methane conversion rate (R_{CH4}) is found to be 6.9×10^{-5} mol g^{-1} s^{-1} at 798 K, which is 2.4 times higher than the methane conversion rate (R_{CH4}) at 723 K. The Arrhenius plot is shown in Fig. S15c.†

The apparent activation energy for the dry reforming of methane reaction on the Co substituted CeO_2 catalyst resulted in 55.18 ± 7.4 kJ mol^{-1}. In the literature, there is no reported apparent activation energy for Co-substituted CeO_2 for the dry reforming of methane reaction. However, the apparent activation energy of various supported Ni catalysts varies from 33.5 to 100 kJ mol^{-1} depending upon the support. A value of 58.6 ± 4.2 kJ mol^{-1} is most frequently reported across the literature for various catalysts.[106] This is in very good agreement with our result.

9 Conclusion

Supported (on) and substituted (in) CeO_2 catalysts are prepared using chemical reduction and solution combustion synthesis methods. The activity of all the catalysts is compared for the dry reforming process. Here the idea is to compare the activity of metallic Co/Ni and ionic Co^{2+}/Ni^{2+} species in both catalysts. Specifically, the catalytic activity in terms of CH_4 conversion over metallic Ni- and Co-supported CeO_2 is around 98% at 800 °C. Small particle size (5–7 nm) could also be one reason for higher methane conversion. In addition to it, CO_2 conversion over metallic Ni- and Co-supported CeO_2 is 84% and 90% at 800 °C. In the substituted system, ionic Co- and Ni-substituted CeO_2, CO_2 conversion is particularly higher than methane conversion. However, Ni-substituted CeO_2 shows the worst stability towards DRM. This catalyst suffers from severe carbon poisoning and sintering which blocks the pores within an hour of reaction. Among all the catalysts, Co-substituted CeO_2 is very active and shows ~90.4% and 97.5% conversion for CH_4 and CO_2 at 800 °C. In addition, it is also the most stable catalyst and shows a H_2/CO ratio of 0.8 which is closer to theoretical ratio one. The H_2/CO ratio

for Ni- and Co-supported CeO_2 is ~0.5 and ~0.6, respectively, at 800 °C. To further know the effects of feed concentration of the reactants over the Co-substituted CeO_2 catalyst a further test at 750 °C for 100 hours was carried out with the mixture $CH_4/CO_2/N_2 = 6/6/8$. Co-substituted CeO_2 exhibited stable CH_4 conversions and only 5.5% deactivation of methane over 100 hours of time on-stream (TOS) was observed. One reason could be the higher concentration of oxygen vacancies which can help remove the deposited carbon by the activation of CO_2 to create O_{ad}, which can eliminate the carbon deposition and maintain high activity and stability of the catalyst over time.

Transient studies indicated the importance of the reaction $CO_2 + C \rightarrow 2CO$, and $C + O_{lattice} \rightarrow CO/CO_2$ in relation to the catalyst's stability and H_2/CO ratio during the DRM reaction. From the transient studies, a plausible reaction pathway can be formulated. For example, the major steps during DRM over Ni-substituted CeO_2 involve methane decomposition to generate H_2 and absorb carbon. The carbon on the catalyst reacts further with CO_2 to produce CO. In contrast, over Co-substituted CeO_2, an additional pathway involving partial methane oxidation may happen because lattice oxygen is actively involved. This additional step is responsible for the catalyst's stability. It is not easy to point out the contribution of the partial oxidation and methane decomposition processes, but Co-substituted CeO_2 has a significant contribution from the oxidation process compared to the other catalysts. Both Ni- and Co-supported catalysts follow similar reaction pathways and behave almost identical which explains that the metal–support interaction is playing a minor role. *Ab initio* calculations on the substituted catalysts confirm that the energy of vacancy formation is significantly lower in Co-substituted CeO_2 as compared to Ni-substituted CeO_2. This confirms that the Co-substituted catalyst favors oxidation due to the higher availability of surface oxygen, while in contrast Ni hinders oxidation by decreasing the availability of surface oxygen for the reaction. Overall, Co substituted CeO_2 is an excellent catalyst because it shows high activity, good stability, and a H_2/CO ratio close to the theoretical one.

Author contributions

Pradeep Kumar Yadav: carried out the synthesis, characterization, catalytic experiments and manuscript writing. Kalyani Patrikar: carried out the DFT calculations. Dr Sudhanshu Sharma: conceptualized and supervised the overall experimental work. Dr Anirban Mondal: supervised the computational work. All the authors contributed to data analysis and writing and gave their approval for final submission.

Conflicts of interest

The authors declare that they have no known competing financial interests or personal relationships that could have appeared to influence the work reported in this paper.

Acknowledgements

This work was supported by Project (MoE/STARS-1/215 and 64T2B). We thank Dr Aditi Haldhar (IIT Mandi) for her help in the XPS analysis. We are thankful for the characterization facilities at Central Instrumentation Facility, IIT Gandhinagar. AM acknowledges PARAM Ananta for the computational facility.

References

1 M. Maestri, D. G. Vlachos, A. Beretta, G. Groppi and E. Tronconi, *AIChE J.*, 2009, **55**, 993–1008.
2 M. Akri, S. Zhao, X. Li, K. Zang, A. F. Lee, M. A. Isaacs, W. Xi, Y. Gangarajula, J. Luo, Y. Ren, Y. T. Cui, L. Li, Y. Su, X. Pan, W. Wen, Y. Pan, K. Wilson, L. Li, B. Qiao, H. Ishii, Y. F. Liao, A. Wang, X. Wang and T. Zhang, *Nat. Commun.*, 2019, **10**, 5181.
3 Y. Song, E. Ozdemir, S. Ramesh, A. Adishev, S. Subramanian, A. Harale, M. Albuali, B. A. Fadhel, A. Jamal, D. Moon, S. H. Choi and C. T. Yavuz, *Science*, 2020, **367**, 777.
4 Z. Liu, D. C. Grinter, P. G. Lustemberg, T. D. Nguyen-Phan, Y. Zhou, S. Luo, I. Waluyo, E. J. Crumlin, D. J. Stacchiola, J. Zhou, J. Carrasco, H. F. Busnengo, M. V. Ganduglia-Pirovano, S. D. Senanayake and J. A. Rodriguez, *Angew. Chem., Int. Ed.*, 2016, **55**, 7455.
5 P. G. Lustemberg, P. J. Ramírez, Z. Liu, R. A. Gutiérrez, D. G. Grinter, J. Carrasco, S. D. Senanayake, J. A. Rodriguez and M. V. Ganduglia-Pirovano, *ACS Catal.*, 2016, **6**, 8184.
6 U. Izquierdo, V. L. Barrio, J. Requies, J. F. Cambra, M. B. Güemez and P. L. Arias, *Int. J. Hydrogen Energy*, 2013, **38**, 7623–7631.
7 A. M. Gaddalla and M. E. Sommer, *Chem. Eng. Sci.*, 1989, **44**, 2825–2829.
8 X. Zhang, J. Deng, M. Pupucevski, S. Impeng, B. Yang, G. Chen, S. Kuboon, Q. Zhong, K. Faungnawakij, L. Zheng, G. Wu and D. Zhang, *ACS Catal.*, 2021, **11**, 12087–12095.
9 Z. Liu, E. Huang, I. Orozco, W. Liao, R. M. Palomino, N. Rui, T. Duchoň, S. Nemšák, D. C. Grinter, M. Mahapatra, P. Liu, J. A. Rodriguez and S. D. Senanayake, *Science*, 2020, **368**, 513.
10 J. Xie, R. Jin, A. Li, Y. Bi, Q. Ruan, Y. Deng, Y. Zhang, S. Yao, G. Sankar, D. Ma and J. Tang, *Nat. Catal.*, 2018, **1**, 889.
11 Z. Jin, L. Wang, E. Zuidema, K. Mondal, M. Zhang, J. Zhang, C. Wang, X. Meng, H. Yang, C. Mesters and F. S. Xiao, *Science*, 2020, **367**, 193.
12 X. L. Tang, B. C. Zhang, Y. Li, Y. D. Xu, Q. Xin and W. J. Shen, *Catal. Today*, 2004, **93–95**, 191.
13 J. R. H. Ross, *Catal. Today*, 2005, **100**, 151–158.
14 G. C. d. Araujo, S. M. d. Lima, J. M. Assaf, M. A. Peña, J. L. G. Fierro and M. do Carmo Rangel, *Catal. Today*, 2008, **133–135**, 129–135.
15 G. S. Gallego, C. Batiot-Dupeyrat, J. Barrault, E. Florez and F. Mondragón, *Appl. Catal., A*, 2008, **334**, 251–258.
16 X. Meng, X. Cui, N. P. Rajan, L. Yu, D. Deng and X. Bao, *Chem*, 2019, **5**, 2296.
17 X. Cui, R. Huang and D. Deng, *EnergyChem*, 2021, **3**, 100050.
18 S. D. Senanayake, J. Evans, S. Agnoli, L. Barrio, T. L. Chen, J. Hrbek and J. A. Rodriguez, *Top. Catal.*, 2011, **54**, 34.

19 S. D. Senanayake, J. A. Rodriguez and J. F. Weaver, *Acc. Chem. Res.*, 2020, **53**, 1488.
20 A. A. Latimer, H. Aljama, A. Kakekhani, J. S. Yoo, A. Kulkarni, C. Tsai, M. Garcia-Melchor, F. Abild-Pedersen and J. K. Nørskov, *Phys. Chem. Chem. Phys.*, 2017, **19**, 3575.
21 D. Pakhare and J. Spivey, *Chem. Soc. Rev.*, 2014, **43**, 7813.
22 R. Horn and R. Schlögl, *Catal. Lett.*, 2015, **145**, 23.
23 H. Schwarz, S. Shaik and J. Li, *J. Am. Chem. Soc.*, 2017, **139**, 17201.
24 C. Fan, Y. A. Zhu, M. L. Yang, Z. J. Sui, X. G. Zhou and D. Chen, *Ind. Eng. Chem. Res.*, 2015, **54**, 5901.
25 T. V. Choudhary and D. W. Goodman, *J. Mol. Catal. A: Chem.*, 2000, **163**, 9.
26 Z. Zhang and X. E. Verykios, *Catal. Lett.*, 1996, **38**, 175–179.
27 M. García-Diéguez, I. S. Pieta, M. C. Herrera, M. A. Larrubia, I. Malpartida and L. J. Alemany, *Catal. Today*, 2010, **149**, 380–387.
28 J. Z. Luo, Z. L. Yu, C. F. Ng and C. T. Au, *J. Catal.*, 2000, **194**, 198–210.
29 S. G. Wang, D. B. Cao, Y. W. Li, J. Wang and H. Jiao, *J. Phys. Chem. B*, 2006, **110**, 9976.
30 C. Carrara, J. Múnera, E. A. Lombardo and L. M. Cornaglia, *Top. Catal.*, 2008, **51**, 98–106.
31 P. Ferreira-Aparicio, C. Márquez-Alvarez, I. Rodríguez-Ramos, Y. Schuurman, A. Guerrero-Ruiz and C. Mirodatos, *J. Catal.*, 1999, **184**, 202–212.
32 K. Sutthiumporn and S. Kawi, *Int. J. Hydrogen Energy*, 2011, **36**, 14435–14446.
33 F. Wang, Y. Wang, L. Zhang, J. Zhu, B. Han, W. Fan, L. Xu, H. Yu, W. Cai, Z. Li, Z. Deng and W. Shi, *Catal. Today*, 2020, **355**, 502–511.
34 F. Wang, L. Xu, J. Zhang, Y. Zhao, H. Li, H. X. Li, K. Wu, G. Q. Xu and W. Chen, *Appl. Catal. B Environ.*, 2016, **180**, 511–520.
35 G. Jones, J. G. Jakobsen, S. S. Shim, J. Kleis, M. P. Andersson, J. Rossmeisl, F. Abild-Pedersen, T. Bligaard, S. Helveg, B. Hinnemann, J. R. Rostrup-Nielsen, I. Chorkendorff, J. Sehested and J. K. Nørskov, *J. Catal.*, 2008, **259**, 147–160.
36 X. Zhang, J. Deng, T. Lan, Y. Shen, Q. Zhong, W. Ren and D. Zhang, *ACS Catal.*, 2022, **12**, 14152–14161.
37 J. Deng, K. Bu, Y. Shen, X. Zhang, J. Zhang, K. Faungnawakij and D. Zhang, *Appl. Catal. B Environ.*, 2022, **302**, 120859.
38 Z. Lian, S. O. Olanrele, C. Si, M. Yang and B. Li, *J. Phys. Chem. C*, 2020, **124**, 5118.
39 J. Carrasco, L. Barrio, P. Liu, J. A. Rodriguez and M. V. Ganduglia-Pirovano, *J. Phys. Chem. C*, 2013, **117**, 8241.
40 R. K. Singha, Y. Tsuji, M. H. Mahyuddin and K. Yoshizawa, *J. Phys. Chem. C*, 2019, **123**, 9788.
41 P. Djinović, J. Batista and A. Pintar, *Int. J. Hydrogen Energy*, 2012, **37**, 2699–2707.
42 J. C. S. Wu and H.-C. Chou, *Chem. Eng. J.*, 2009, **148**, 539–545.
43 P. Ferreira-Aparicio, A. Guerrero-Ruiz and I. Rodríguez-Ramos, *Appl. Catal., A*, 1998, **170**, 177–187.
44 G. K. Reddy, S. Loridant, A. Takahashi, P. Delichère and B. M. Reddy, *Appl. Catal., A*, 2010, **389**, 92–100.
45 V. A. Sadykov, E. L. Gubanova, N. N. Sazonova, S. A. Pokrovskaya, N. A. Chumakova, N. V. Mezentseva, A. S. Bobin, R. V. Gulyaev, A. V. Ishchenko, T. A. Krieger and C. Mirodatos, *Catal. Today*, 2011, **171**, 140–149.
46 F. Wang, K. Han, W. Yu, L. Zhao, Y. Wang, X. Wang, H. Yu and W. Shi, *ACS Appl. Mater. Interfaces*, 2020, **12**, 35022–35034.
47 A. S. Al-Fatesh, A. H. Fakeeha, A. A. Ibrahim and A. E. Abasaeed, *Int. J. Hydrogen Energy*, 2021, **46**, 3780–3788.
48 C. M. Damaskinos, M. A. Vasiliades and A. M. Efstathiou, *Appl. Catal., A*, 2019, **579**, 116–129.
49 M. A. Vasiliades, C. M. Damaskinos, P. Djinović, A. Pintar and A. M. Efstathiou, *Catal. Commun.*, 2023, **178**, 106674.
50 C. M. Damaskinos, J. Zavašnik, P. Djinović and A. M. Efstathiou, *Appl. Catal. B Environ.*, 2021, **296**, 120321.
51 M. A. Vasiliades, C. M. Damaskinos, P. Djinović, A. Pintar and A. M. Efstathiou, *Catal. Commun.*, 2021, **149**, 106237.
52 A. G. S. Hussien, C. M. Damaskinos, A. A. Dabbawala, D. H. Anjum, M. A. Vasiliades, M. T. A. Khaleel, N. Wehbe, A. M. Efstathiou and K. Polychronopoulou, *Appl. Catal. B Environ.*, 2022, **304**, 121015.
53 M. A. Vasiliades, P. Djinović, A. Pintar, J. Kovač and A. M. Efstathiou, *Catal. Sci. Technol.*, 2017, **7**, 5422–5434.
54 J. Nakamura, K. Aikawa, K. Sato and T. Uchijima, *Catal. Lett.*, 1994, **25**, 265–270.
55 V. A. Tsipouriari, A. M. Efstathiou, Z. L. Zhang and X. E. Verykios, *Catal. Today*, 1994, **21**, 579–587.
56 K. Han, S. Wang, N. Hu, W. Shi and F. Wang, *ACS Appl. Mater. Interfaces*, 2022, **14**, 23487–23495.
57 Y. Shi, K. Han and F. Wang, *Inorg. Chem.*, 2022, **61**, 15619–15628.
58 K. Han, S. Wang, Q. Liu and F. Wang, *ACS Appl. Nano Mater.*, 2021, **4**, 5340–5348.
59 C. M. Damaskinos, M. A. Vasiliades, V. N. Stathopoulos and A. M. Efstathiou, *Catalysts*, 2019, **9**, 621.
60 F. Zhang, Z. Liu, S. Zhang, N. Akter, R. M. Palomino, D. Vovchok, I. Orozco, D. Salazar, J. A. Rodriguez, J. Llorca, J. Lee, D. Kim, W. Xu, A. I. Frenkel, Y. Li, T. Kim and S. D. Senanayake, *ACS Catal.*, 2018, **8**, 3550–3560.
61 Y. Tang, Y. Wei, Z. Wang, S. Zhang, Y. Li, L. Nguyen, Y. Li, Y. Zhou, W. Shen, F. F. Tao and P. Hu, *J. Am. Chem. Soc.*, 2019, **141**, 7283–7293.
62 K. C. Patil, M. S. Hegde, T. Rattan and S. T. Aruna, *Chemistry of Nanocrystalline Oxide Materials*, World Scientific, 2008.
63 A. Bisht, A. Sihag, A. Satyaprasad, S. S. Mallajosyala and S. Sharma, *Catal. Lett.*, 2018, **148**, 1965–1977.
64 A. Bisht, P. Zhang, C. Shivakumara and S. Sharma, *J. Phys. Chem. C*, 2015, **119**, 14126–14134.
65 J. Hutter, M. Iannuzzi, F. Schiffmann and J. VandeVondele, *Wiley Interdiscip. Rev. Comput. Mol. Sci.*, 2014, **4**, 15–25.
66 J. P. Perdew, K. Burke and M. Ernzerhof, *Phys. Rev. Lett.*, 1996, **77**, 3865.
67 K. R. Hahn, M. Iannuzzi, A. P. Seitsonen and J. Hutter, *J. Phys. Chem. C*, 2013, **117**, 1701–1711.
68 S. Wang, J. Wang and H. Xin, *Green Energy Environ.*, 2017, **2**, 168–171.

69 S. Goedecker, M. Teter and J. Hutter, *Phys. Rev. B: Condens. Matter Mater. Phys.*, 1996, **54**, 1703–1710.
70 K. Han, W. Yu, L. Xu, Z. Deng, H. Yu and F. Wang, *Fuel*, 2021, **291**, 120182.
71 C. Tang, J. Li, X. Yao, J. Sun, Y. Cao, L. Zhang, F. Gao, Y. Deng and L. Dong, *Appl. Catal., A*, 2015, **494**, 77–86.
72 M. Radlik, M. Adamowska-Teyssier, A. Krztoń, K. Kozieł, W. Krajewski, W. Turek and P. Da Costa, *C. R. Chim.*, 2015, **18**, 1242–1249.
73 S. Zhang, S. Muratsugu, N. Ishiguro and M. Tada, *ACS Catal.*, 2013, **3**(8), 1855–1864.
74 E. Heracleous, A. F. Lee, K. Wilson and A. A. Lemonidou, *J. Catal.*, 2005, **231**, 159–171.
75 A. M. Tarditi, M. F. Mori and L. M. Cornaglia, *Top. Catal.*, 2019, **62**, 822–837.
76 A. M. Tarditi, N. Barroso, A. E. Galetti, L. A. Arrúa, L. Cornaglia and M. C. Abello, *Surf. Interface Anal.*, 2014, **46**, 521–529.
77 W. Zou, C. Ge, M. Lu, S. Wu, Y. Wang, J. Sun, Y. Pu, C. Tang, F. Gao and L. Dong, *RSC Adv.*, 2015, **5**, 98335–98343.
78 S. Dutta, A. Indra, Y. Feng, T. Song and U. Paik, *ACS Appl. Mater. Interfaces*, 2017, **9**, 33766–33774.
79 N. S. Arul and D. Mangalaraj, *Cryst. Res. Technol.*, 2015, **50**, 532–537.
80 M. Greluk, M. Rotko, G. Słowik and S. Turczyniak-Surdacka, *J. Energy Inst.*, 2019, **92**, 222–238.
81 A. Jha, D.-W. Jeong, Y.-L. Lee, I. W. Nah and H.-S. Roh, *RSC Adv.*, 2015, **5**, 103023–103029.
82 H. Sohn, G. Celik, S. Gunduz, D. Dogu, S. Zhang, J. Shan, F. F. Tao and U. S. Ozkan, *Catal. Lett.*, 2017, **147**, 2863–2876.
83 D. Jampaiah, P. Venkataswamy, V. E. Coyle, B. M. Reddy and S. K. Bhargava, *RSC Adv.*, 2016, **6**, 80541–80548.
84 Z. Wu, M. Li, J. Howe, H. M. Meyer and S. H. Overbury, *Langmuir*, 2010, **26**, 16595–16606.
85 R. O. da Fonseca, A. R. Ponseggi, R. C. Rabelo-Neto, R. C. C. Simões, L. V. Mattos and F. B. Noronha, *J. CO2 Util.*, 2022, **57**, 101880.
86 J. Wu, J. Gao, S. Lian, J. Li, K. Sun, S. Zhao, Y. D. Kim, Y. Ren, M. Zhang, Q. Liu, Z. Liu and Z. Peng, *Appl. Catal. B Environ.*, 2022, **314**, 121516.
87 A. Bendieb Aberkane, M. P. Yeste, D. Fayçal, D. Goma and M. Á. Cauqui, *Materials*, 2019, **12**(20), 3436.
88 I. Luisetto, S. Tuti and E. Di Bartolomeo, *Int. J. Hydrogen Energy*, 2012, **37**, 15992–15999.
89 S. Xu, X. Yan and X. Wang, *Fuel*, 2006, **85**, 2243–2247.
90 S. M. de Lima, A. M. da Silva, L. O. O. da Costa, U. M. Graham, G. Jacobs, B. H. Davis, L. V. Mattos and F. B. Noronha, *J. Catal.*, 2009, **268**, 268–281.
91 L. F. Liotta, G. Di Carlo, G. Pantaleo, A. M. Venezia and G. Deganello, *Appl. Catal. B Environ.*, 2006, **66**, 217–227.
92 V. Ferrer, A. Moronta, J. Sánchez, R. Solano, S. Bernal and D. Finol, *Catal. Today*, 2005, **107–108**, 487–492.
93 M. Boudart and H. S. Hwang, *J. Catal.*, 1975, **39**, 44–52.
94 H. Lieske and J. Voelter, *J. Phys. Chem.*, 1985, **89**, 1841–1842.
95 U. Oemar, Y. Kathiraser, L. Mo, X. K. Ho and S. Kawi, *Catal. Sci. Technol.*, 2016, **6**, 1173–1186.
96 Y. Lou, M. Steib, Q. Zhang, K. Tiefenbacher, A. Horváth, A. Jentys, Y. Liu and J. A. Lercher, *J. Catal.*, 2017, **356**, 147–156.
97 L. Wang and F. Wang, *Energy Fuels*, 2022, **36**, 5594–5621.
98 J. H. Lehman, M. Terrones, E. Mansfield, K. E. Hurst and V. Meunier, *Carbon*, 2011, **49**, 2581–2602.
99 D. Bom, R. Andrews, D. Jacques, J. Anthony, B. Chen, M. S. Meier and J. P. Selegue, *Nano Lett.*, 2002, **2**, 615–619.
100 K. Nagaoka, K. Seshan, K.-i. Aika and J. A. Lercher, *J. Catal.*, 2001, **197**, 34–42.
101 K. Nagaoka, K. Aika, K. Seshan and J. A. Lercher, in *Studies in Surface Science and Catalysis*, ed. E. Iglesia, J. J. Spivey and T. H. Fleisch, Elsevier, 2001, vol. 136, pp. 129–134.
102 H. Ay and D. Üner, *Appl. Catal. B Environ.*, 2015, **179**, 128–138.
103 Y. Li, B. Zhang, X. Tang, Y. Xu and W. Shen, *Catal. Commun.*, 2006, **7**, 380–386.
104 G. Pantaleo, V. L. Parola, F. Deganello, R. K. Singha, R. Bal and A. M. Venezia, *Appl. Catal. B Environ.*, 2016, **189**, 233–241.
105 M. F. Mark and W. F. Maier, *J. Catal.*, 1996, **164**, 122–130.
106 K. Song, M. Lu, S. Xu, C. Chen, Y. Zhan, D. Li, C. Au, L. Jiang and K. Tomishige, *Appl. Catal. B Environ.*, 2018, **239**, 324–333.

